

Reply to anonymous Referee #1

We would like to thank the anonymous Referee #1 for his/her detailed and constructive review. The comments and suggestions were very helpful and significantly contributed to improving the clarity, robustness, and overall quality of the manuscript.

In the following, analytical replies are provided to each of the reviewer's comments. Reviewer's comments are written in bold font. Line numbers, when provided, refer to the new version with track changes.

The manuscript “PV power modelling using solar radiation from ground-based measurements and CAMS: Assessing the diffuse component related uncertainties leveraging the Global Solar Energy Estimator (GSEE)” by Nikolaos Papadimitriou et al. focuses on the exploitation of the impact of the partitioning of the global horizontal irradiance (GHI) in its direct and diffuse components on the PV power production by simulations with the widely used Global Solar Energy Estimator (GSEE) model. The solar irradiance, air temperature, aerosol optical depth input sources are the BSRN and AERONET measurements from 5 sites in Europe, North Atlantic Ocean and Sahara desert and the CAMS model. The diffuse fraction (DF), being rarely measured except in a limited number of sites, is estimated within the GSEE through the logistic Boland-Ridley-Lauret (BRL) model, based on the clearness index as the main parameter. The effects of different cloud cover and aerosol optical depth on DF, and the corresponding impact on the simulation of power production is evaluated for fixed and 2-axis tracking PV systems based on c-Si and CdTe technology. The effects on different timescales are also explored. Finally, an assessment of the financial impacts deriving from evaluating the DF of desert dust from the BRL model compared to the measured GHI components, for a hypothetical PV solar farm around Tamanrasset is provided.

The main conclusion is that the best agreement in DF estimation with BRL model and ground-based measurements is for cloud-free and very low to moderate aerosol, i.e. for the simplest atmospheric conditions to be modelled. The worst situation for a reliable power production estimation is for partially cloudy skies. In sites impacted by high dust load, the BRL underestimated the DF and the power generation is overestimated.

We would like to thank the reviewer for his/her time and comments.

General comments

While it is clear that the GSEE is widely used and the BRL model is optimized for both the Northern and Southern Hemispheres, I suspect it is not the best model for analyzing the effects of aerosols on the GHI partition, as the clearness index is mostly influenced by cloudiness and the reader is not informed about how the aerosols are accounted for. The authors should address this aspect, which is a key point in the development of the work.

as well as discuss similar works, if any, dealing with this topic.

Despite the large amount of calculations done in this work, the results are not valued by an adequate discussion, both in qualitative and quantitative terms. As a general comment I suggest quantifying the results in the text (Results and Conclusions sections) and not leaving the values only in the supplementary material.

The authors do not cite in the Introduction any previous paper dealing with the estimation of PV power generation under different cloudiness and/or aerosol load conditions, nor compare any of their results with previous works. If a similar work is not found in literature, this aspect, which increases the importance of this study, should be emphasized both in the introduction and in the conclusions.

Overall, I recommend a major revision of the key points before publication.

Reply

We acknowledge the limitations of the BRL model, especially regarding the effects of aerosols on GHI partition. However, it constitutes a key submodule of the GSEE library, as it is integrated within the internal processing chain of the climate data interface, a feature that plays a central role in the applicability of GSEE to climate-driven assessments. Some text has been added in the Introduction to clarify this (lines 84-86)

Moreover, following an extensive review of the relevant literature indicates that, despite the large number of studies discussing the role of aerosols and clouds on the amount of and the distribution of the solar irradiance that reaches the Earth's surface (Fountoulakis et al., 2021; Kosmopoulos et al., 2018; Papachristopoulou et al., 2022; Amiridis et al., 2024; Kosmopoulos et al., 2017; Calastrini et al., 2024; Kouklaki et al., 2023), there is a lack of studies addressing reliability of PV power simulations under diverse atmospheric conditions due to inaccuracies in the representation of the diffuse component in PV power models. Furthermore, we were not able to find any study examining the reliability of CAMS radiation data for PV power potential assessments. Some relevant text has been added both the Introduction and the Conclusions (lines 98-102 and lines 586-589)

In addition, the manuscript has been revised to include a more detailed quantitative discussion of the evaluation in Sections 3.3 – 3.5, and some tables have been transferred from the Supplement to the main text.

REFERENCES

Amiridis, V., Kazadzis, S., Gkikas, A., Voudouri, K. A., Kouklaki, D., Koukouli, M.-E., Garane, K., Georgoulias, A. K., Solomos, S., Varlas, G., Kampouri, A., Founda, D., Psiloglou, B. E., Katsafados, P., Papachristopoulou, K., Fountoulakis, I., Raptis, P.-I., Georgiou, T., Gialitaki, A., ... Zerefos, C. (2024). Natural aerosols, gaseous precursors and their impacts in Greece: A review from the remote sensing perspective. *Atmosphere*, 15(7), 753. <https://doi.org/10.3390/atmos15070753>

Calastrini, F., Messeri, G., & Orlandi, A. (2024). Long-range mineral dust transport events in Mediterranean countries. *Air*, 2(4), 444–467. <https://doi.org/10.3390/air2040026>

Kosmopoulos, P. G., Kazadzis, S., Taylor, M., Athanasopoulou, E., Speyer, O., Raptis, P. I., Marinou, E., Proestakis, E., Solomos, S., Gerasopoulos, E., Amiridis, V., Bais, A., & Kontoes, C. (2017). Dust impact on surface solar irradiance assessed with model simulations, satellite observations and ground-based measurements. *Atmospheric Measurement Techniques*, 10(7), 2435–2453. <https://doi.org/10.5194/amt-10-2435-2017>

Kosmopoulos, P., Kazadzis, S., El-Askary, H., Taylor, M., Gkikas, A., Proestakis, E., Kontoes, C., & El-Khayat, M. (2018). Earth-Observation-based estimation and forecasting of particulate matter impact on solar energy in Egypt. *Remote Sensing*, 10(12), 1870. <https://doi.org/10.3390/rs10121870>

Kouklaki, D., Kazadzis, S., Raptis, I.-P., Papachristopoulou, K., Fountoulakis, I., & Eleftheratos, K. (2023). Photovoltaic spectral responsivity and efficiency under different aerosol conditions. *Energies*, 16(18), 6644. <https://doi.org/10.3390/en16186644>

Papachristopoulou, K., Fountoulakis, I., Gkikas, A., Kosmopoulos, P. G., Nastos, P. T., Hatzaki, M., & Kazadzis, S. (2022). 15-year analysis of direct effects of total and dust aerosols in solar radiation/energy over the Mediterranean Basin. *Remote Sensing*, 14(7), 1535. <https://doi.org/10.3390/rs14071535>

Specific comments

Lines 67-72: since the use of an empirical model constitutes a relevant part of the work, I suggest to detail a little the description of these models and in particular the

description of the BRL model, for example by mentioning here the variables that are used to derive the DF.

Reply

Some text added in order to highlight the innovative formulation besides the BRL model (lines 70-81)

Line 71: some information about the BRL model should be provided, since the model is widely used in the paper. Is this the only model for DF estimation incorporated in the GSEE?

Reply

GSEE includes only the BRL model. Although the user in its single usage (modelling a PV plant with hourly time-series data in a specified project location) has the option to use other diffuse fraction models (such as those included in pvlib), the climate data interface tool is designed for deploying exclusively the BRL implementation.

Some text added to clarify this (lines 127-131).

Table 3 with the libRadtran input parameters is somehow unclear. The SZA input is “with step 90°”: what do the authors mean? In addition, is the wavelength dependence of the surface albedo, SSA and gg accounted for? Finally, I suggest “integrated water vapor” instead of “water vapor”.

Reply

The reference to SZA input was a transcription error that was introduced during the manuscript revision. As the BRL model requires hourly input data at exact hourly timestamps for at least one full day, we used the libRadtran option to set as input datetime accompanied with the coordinates instead of SZA directly. After, in the analysis we computed the corresponding SZA values. In section 3.2, we stated that we chose the summer solstice as a representative day with sufficient number daylight hours.

Regarding the wavelength dependence of SSA and gg is not accounted for in the present analysis. In the present, this dependence is not explicitly accounted for, as the objective is not a fully spectrally resolved radiative transfer analysis, but rather to investigate the differences associated with some representative SSA values.

We accepted also the suggestion for adding the word Integrated before Water Vapor.

Lines 290-295 and Figure 2: the comparison of the DF from the BSRN measurements and the BRL model is tricky. Do the differences for $SZA > 60^\circ$ increase because of the difficulty of the model in estimating the DF for high SZAs? The bottom of Figure 2 shows that this happens for cloud-free conditions above 70° (not 60° SZA as said in the text) and not for all sites: Izana do not show the SZA dependence. It appears also for the cleanest conditions, i.e. for $AOD500 \leq 0.05$.

In my opinion this deserves a little bit more investigation, instead of simply limiting the comparison to SZAs below 60° , as in Figure 3.

Reply

We agree that the shift becomes observable within the range of 60-70 degrees. However, the specific point at which SZA starts to affect cannot be identified with precision. Therefore, a value of 60 degrees adopted as reference limit for practical reasons related to solar energy production applications, as above this value the low absolute irradiance levels contribute less to total energy yield. Moreover, we investigated this in section 3.2 in the sensitivity, where under clear sky conditions the shift arising closer to 70 degrees.

In Izana, there is the influence of altitude, where the levels of the diffuse irradiance are significantly lower.

The difficulty of the model in estimating the diffuse fraction for high SZA values may arise from the symmetry of a typical daily profile of the diffuse fraction and the hourly clearness, as the model requires full-day input data for hourly clearness. This is confirmed also by the sensitivity analysis, as the model has similar behavior.

Some clarifying text has been added.

Line 326: under overcast conditions the BRL DF takes a range of values, approximately from 0.6 to 1, while the BSRN DF is close to 1. This means that even for homogeneous sky conditions, isotropic radiation the BRL model is not capable of providing reliable DF estimates. The authors could also refer to the 3D variability of cloud properties, whose effect cannot be accounted for by a model like BRL.

Reply

The vast majority of cases where the BRL diffuse fraction is below 0.8 while the observed is close to 1 correspond to periods involving rapid transitions between partly cloudy and overcast skies, occurring either during the hour itself or immediately before or after it. These discrepancies can be mainly attributed to limitations of the DNI-based characterization methodology for cloudiness.

Moreover, the presence of aerosols can amplify these discrepancies. Even under cloudy conditions, aerosol may coexist and contribute, despite the difficulty to be measured and quantified.

Furthermore, a limited number of cases identified during intense dust events at Tamanrasset and Izana, where the reduction of DNI was so pronounced that the applied DNI-based criterion classified these conditions as overcast.

However, we did not further investigate these inconsistencies, as the energy production levels during such periods are very low.

Some clarifying text has been added (lines 327-337).

Section 3.2: the dependence on latitude and altitude is not discussed, although presented in Figure 5.

The results show that for totally scattering aerosols (SSA=1) the BRL model underestimates the DF, while for absorbing aerosols (SSA=0.7) is overestimates the DF.

The authors may briefly discuss the results of the sensitivity analysis in terms of how the BRL logistic model treats the aerosol-radiation interactions. The model does not explicitly include the aerosol optical properties, but incorporates their effects into the clearness index, together with those exerted by the clouds, which are by no means larger. In this section, instead, the authors examine in detail how aerosols influence the partitioning of GHI into direct and diffuse components, and the results obtained with the BRL model are strongly biased, as expected. This is also a consequence of how the model was conceived, in particular of the data with which the relationship between the DF and the geometric, meteorological and atmospheric variables were determined.

Reply

Some clarifying text added to discuss the effect of altitude and altitude, and to emphasize on the range of the discrepancies as an outcome of the effect of aerosol with different optical properties.

Section 3.3: the authors should comment the results presenting the quantification of the differences in power production derived from using only GHI or GHI and DHI as GSEE model input. Not all sites and all atmospheric conditions have to be considered, but at least for two sites with different characteristics, such as Izana and Lindenberg, for fixed and 2-axis tracking systems.

Reply

Some text has been added, as well as Tables with the computed indices for Carpentras and Tamanrasset (as representative locations) have been transferred from the supplement to the manuscript.

Lines 492-494: the data gaps are in the GHI data and/or in the irradiance components? Can the author suggest a reason for these gaps? Does using a less stringent condition on the number of days per month (for example 15 days) allow for a less fragmented annual evolution?

Reply

The data gaps occur mainly close to the solar noon during the summer months and arise from removing data through the quality control checks applied in the BSRN. Rejection of the data during the BSRN QC procedure is possibly related to operational issues at the station. Even though the data gaps are in most cases less than 2-3 hours, they may affect the BRL performance throughout these days. Thus, these days have been removed from the analysis.

Lines 495-501: I find it very useful to present the differences also in percentage, referred to the energy production obtained using GHI and DHI as a reference.

Reply

A Figure showing the percentage differences added in the supplement. Some discussion relative to the new figure has been added in the manuscript (lines 499-501).

Section 3.5: more details about the CAMS data selection are needed. For example: the authors say that the CAMS solar radiation data are adapted to the investigated sites, but how is this done? By interpolation, by considering the nearest CAMS grid point? Moreover, the Izana site is excluded from the analysis because the altitude of the site is

not directly comparable to the model vertical grid. For this reason, it is useful to know the CAMS 3D spatial grid and to add it in Section 2.3.

Another missing point is the quantification of the irradiance differences on power production, a qualitative discussion is not sufficient.

Finally, the authors should refer to previous papers, if any, dealing with the use of CAMS irradiance data for modelling PV potential power production.

Reply

For the data selection we used the “CAMS solar radiation time-series” product, where the user sets as input the coordinates as well as the altitude of a specific location, and then the output data are offered in ASCII format. Therefore, the interpolation methodology is integrated to the CAMS product algorithm. Some text added to clarify this in section 2.3.

Some text has also been added to discuss quantitatively the validation as well as to highlight the novelty of this work, as we could not find studies directly examining CAMS performance for PV power modelling.

Conclusions: should summarize the main results and report some numerical data, which otherwise are only relegated in the supplementary material. For example, the results may be evaluated for two or three sites with different characteristics in terms of latitude and aerosol regimes. I suggest reporting the impact on the power generation not only as absolute values, but also as percent, to facilitate understanding. In addition, even if the results pertaining to the panels with CdTe technology are not different from those obtained for c-Si panels, they should be briefly recalled.

When discussing the assessment of the financial impacts of the desert dust effects at Tamanrasset, the authors should clearly address that the analysis considers the differences in diffuse function derived from the measurements and calculated by the model. The sentence in lines 474-476 “Therefore, site assessments that do not account for the impact of desert dust aerosols may overestimate financial performance....” may be misleading, as it may be interpreted as the assumption that desert dust is not accounted for in the model simulations. I suggest reformulating the sentence.

Reply

We tried to improve the conclusions section as recommended by the reviewer.

Technical corrections

We thank the reviewer for the detailed comments and suggestions. All minor editorial, typographical, and wording-related comments (e.g., punctuation, wording clarifications, terminology corrections) have been carefully addressed and incorporated into the revised manuscript.

Responses to the comments requiring further clarification are provided below.

Line 142: can the authors quantify how much is the uncertainty on using a fixed surface albedo of 0.3?

Reply

The default GSEE value of 0.3 can be considered as representative for most types of surfaces (e.g., the surface albedo for urban landscapes, desert, and green grass is usually between 0.2 and 0.4). There are of course darker surfaces (e.g., forests, asphalt).

In the context of past studies (see reply to reviewer 1 in Papachristopoulou et al., 2024: <https://doi.org/10.5194/amt-2023-110-AC1>), we have investigated the sensitivity of the GHI irradiance to the surface albedo under various conditions (see the Figures below). For SZAs below 75° and under clear sky conditions, changing surface albedo by 10% changes the GHI by less than 1% (i.e., the difference is within the uncertainty range of the ground-based measurements). Under cloudy conditions the % differences are larger (i.e., ~ 5% for a 10% change in surface albedo for Cloud Optical Thickness of 12), but under such conditions the amount of PV power potential is small. Since very high surface albedo values are rare at the latitudes where the study is focused, and differences from the default value are generally smaller than 0.2, we decided to use the default surface albedo value. The manuscript has been also updated with this information (see lines 142-145)

Line 159: is this reference correctly cited?

Reply

Yes, the reference is correctly cited. It corresponds to an online source from the official GSEE model website, which has been cited accordingly in the revised manuscript.

Table 1: is it necessary? In my opinion the text description is exhaustive.

Reply

We have retained Table 1, as it provides a concise overview of the input parameters used in the GSEE model for the purposes of this study, complementing the textual description and improving clarity for the reader.

Line 198: is it “daily” or “hourly”?

Reply

It is daily, as this refers to the pre-processing of the data that used as input to the climate interface

Lines 256-257: I suggest to include a sentence on how the solar radiation is estimated in CAMS and the 3D spatial resolution, an important information for the CAMS data selection operated for the analysis described in Section 3.5.

Reply

Additional text has been added to clarify that the CAMS solar radiation time-series product is used. The description now briefly outlines how the data are retrieved, including the use of location coordinates and station altitude as inputs (lines 261-263).

Line 367: maybe “ground altitude”?

Reply

This was a typographical error, which has been corrected in the revised manuscript. The correct value is 0.1 km, rather than “0,1”.

Line 598: express the power overestimation also in percent number and the site where this is observed (should be Tamanrasset). Is the 49.2 Wh/kWp/hour on hourly value? I could not find this number in the supplementary material tables.

Reply

This issue was caused by a typographical error and the inadvertent omission of several rows from the table, which have now been corrected in the revised manuscript. The value of 49.2

Wh/kW_p per hour refers to an hourly estimate for the Tamanrasset site and is now correctly reported in Table 4. The relative mean bias error (rMBE) is expressed percentage terms.

Line 613: Table 4 is not present.

Reply

Table 4 had been removed during a previous revision and transferred to the Supplementary Material; however, the reference in the main text was not updated accordingly. In the revised manuscript, Table 4 has been reinstated in the main text and the reference has been corrected.

Figure 6: bottom graphs. Why the data produced with only GHI for Izana seem to be cut around 900 Wh/kW_p per hour?

Reply

The PV systems considered in this study have a nominal capacity of 1 kW_p. The PV model applies a default system loss factor of 10%. This effectively limits the maximum achievable power output to approximately 90% of the nominal capacity (i.e., around 900 W/kW_p). This effect becomes apparent at the Izaña site due to its low latitude combined with its specific geographical and atmospheric conditions, which lead to high irradiance levels. As a result, the simulated PV output appears capped around 900 Wh/kW_p per hour when only GHI is used.

Table S2: the metrics for high and very high aerosol load are missing.

Reply

The issue was due to missing rows in the previous version of Table S2. The table has been corrected and is now included as Table 4 in the revised manuscript, containing all metrics for low, high, and very high aerosol load conditions.

Reply to anonymous Referee #2

We would like to thank the anonymous Referee #2 for the careful evaluation of the manuscript and the helpful comment and suggestions. The reviewer's remarks were valuable in improving the presentation, consistency, and technical clarity of the study, and helped us to address several points that required further clarification.

Detailed responses to the reviewer's comments are provided below. The reviewer's comments are reported in bold font, and line numbers, when provided, refer to the revised manuscript with track changes enabled.

This manuscript presents a comprehensive assessment of the impact of uncertainty in the diffuse component of solar radiation on the prediction of photovoltaic energy production using the Global Solar Energy Estimator (GSEE) and different data sources. This analysis includes categorization based on sky and aerosol conditions. The manuscript is well-organized and well-written, and the topic is worthy of study. However, there are some aspects that still need clarification or improvement.

We would like to thank the reviewer for his/her time and comments.

The specific comments are as follows:

1. Throughout the document, the existence of a reflected component of solar radiation on a tilted surface is not explicitly mentioned. It is understood that the authors include this component in the "diffuse" radiation, although, usually, in much literature, diffuse (sky) and reflected components are treated separately. Furthermore, the document does not specify which transposition model is used to determine solar irradiance on the inclined surface (in the same way that the separation model included in GSEE for estimating the diffuse fraction is mentioned). Several transposition models exist that treat diffuse sky irradiance in different ways, from the simplest, which considers it isotropic, to the more elaborate ones that separate the sky into different regions (background diffuse, circumsolar region, horizon brightening). This is important because fixed systems with different tilt angles and two-axis tracking systems are studied in different locations, and specifying which transposition model was used will allow for a better discussion and understanding of the results.

Reply

The GSEE package includes the submodule “trigon”, which contains a set of functions for computing the in-plane irradiance. These functions are based on trigonometric formulations, that account of the surface albedo, thereby including the ground-reflected component of solar radiation.

The main submodule of the GSEE library used to simulate the electric output of a PV panel requires as input the separated irradiance data (GHI, and diffuse fraction). Subsequently, it internally calls the trigon transposition model to compute the plane-of-array irradiance, which is then used to estimate the PV power output.

In contrast to BRL submodule – where apart from the climate data interface, alternative diffuse fraction models can be selected by the user in single-site application – the transposition model in GSEE is fixed and cannot be modified by the user.

Some text has been added (lines 133-137)

2. Line 193 states that the data were "resampled to hourly", but this is unclear and needs clarification. Is an hourly average calculated? Refer also to Line 260 where hourly values are mentioned. The BRL model is based on irradiance values integrated over a one-hour period (Ridley et al., 2010). Please clarify. Regarding the AERONET data, how were the values treated given that the raw data does not have a defined periodicity?

Reply

The resampling to hourly resolutions refers to the calculation of hourly mean values. The implementation of the BRL model included within the GSEE requires full-days timeseries of the hourly clearness index. For this purpose, the mean GHI of each hour is divided with the TOA on horizontal plane, which calculated as follows: $\text{Solar_Constant}(\text{Day_of_Year}) * \cos(\text{SZA})$, where SZA is evaluated at the midpoint of the hour.

Regarding the AERONET data, although the original measurements do not have a fixed temporal periodicity, the data are resampled by computing hourly mean values from all available observations within each hour. This procedure ensures temporal consistency with the hourly irradiance and BRL model inputs.

The calculation of hourly mean values is clarified in the revised text.

3. In Line 211: How the values of $0 < \text{SV} < 1$ for partly cloudy conditions are determined? This is not clear. Also, if using a value of SV between 0 and 1 to

characterize the intra-hour conditions then the value of irradiance must be hourly mean values (see also comment 2). Please clarify this aspect and justify the use of SV compared to the use of other indicators, such as the clear-sky index (not the clearness index), defined as the ratio of actual irradiance to irradiance for clear sky conditions from a suitable model, for example. This also relates to what is said in Line 290, where the use of cameras is suggested to overcome the issue of small and scattered clouds within the sky dome that enhances the diffuse component while not blocking the direct normal irradiance. There are other effective methods for identifying sky conditions. Please comment and clarify.

Reply

Representing the effect of cloudiness was challenging, as it requires the deployment of several observations. However, the DNI-based formulation aims to provide an indicative measure of the intra-hour cloudiness conditions. Alternative approaches, such as the clear-sky index or the Cloud Modification Factor require estimates of the clear sky GHI, which also introduce uncertainty. Some text added in lines 202 to 208.

4. In Line 220, regarding the AERONET data, please clarify "... data were resampled at hourly intervals ..." in view of comment 2 above.

Reply

Some clarifying text has been added.

5. In lines 234 and 247, there appear to be some typos (an extra "c" and "my", respectively).

Reply

All the typos have been removed.

6. In Figure 3: the represented data is only for SZA < 60, correct? Please, confirm this and mention it in the figure caption.

Reply

Yes, we confirm that the figures is for SZA < 60. The figure caption revised to include this information.

7. In Figure 8 and associated text, the reason why using a 30-days moving average is not clear. Is a centered moving average used? Please clarify, also regarding the data gaps which, up to this point in the document, were not evident (may be including in Table 2 this information will help).

Reply

A centered 30-day moving average is used in Figure 8. The purpose of applying the moving average is to reduce short-term variability and highlight the underlying temporal behavior of the analyzed quantities, facilitating a clearer comparison of trends.

The data gaps occur mainly around solar noon and arise from measurements removed during the application of the BSRN quality control checks. Although these gaps are, in most cases, shorter than 2–3 hours, they may affect the BRL model performance for the corresponding days. This information has now been clarified in the revised text (lines 189–192).

1 **PV power modelling using solar radiation from ground-based**
2 **measurements and CAMS: Assessing the diffuse component related**
3 **uncertainties leveraging the Global Solar Energy Estimator (GSEE)**

4 Nikolaos Papadimitriou^{1,2}, Ilias Fountoulakis², Antonis Gkikas², Kyriakoula
5 Papachristopoulou³, Andreas Kazantzidis¹, Stelios Kazadzis³, Stefan Pfenninger⁴, John
6 Kapsomenakis², Kostas Eleftheratos^{5,6}, Athanassios A. Argirou¹, Lionel Doppler⁷, and
7 Christos S. Zerefos^{2,6,8,9}

8 ¹Department of Physics, University of Patras, 26500 Patras, Greece

9 ²Research Centre for Atmospheric Physics and Climatology, Academy of Athens, 11521 Athens,
10 Greece

11 ³Physikalisch-Meteorologisches Observatorium Davos, World Radiation Center (PMOD/WRC), 7260
12 Davos, Switzerland

13 ⁴Faculty of Technology, Policy, and Management (TPM), Delft University of Technology, 2628 BX
14 Delft, the Netherlands

15 ⁵Department of Geology and Geoenvironment, National and Kapodistrian University of Athens,
16 15784 Athens, Greece

17 ⁶Biomedical Research Foundation, Academy of Athens, 11527 Athens, Greece

18 ⁷Deutscher Wetterdienst, Meteorologisches Observatorium Lindenberg – Richard Assman
19 Observatorium (DWD, MOL-RAO), 15848 Lindenberg (Tauche), Germany

20 ⁸Navarino Environmental Observatory (N.E.O.), 24001 Messinia, Greece

21 ⁹Mariolopoulos-Kanaginis Foundation for the Environmental Sciences, 10675 Athens, Greece

22 Corresponding author: Nikolaos Papadimitriou (npapadimitriou@academyofathens.gr, Vasilissis
23 Sofias 79, 11521 Athens, Greece)

24 **Abstract**

25 Accurate PV power production modelling requires precise knowledge of the distribution of solar
26 irradiance among its direct and diffuse components. Since this information is rarely available, this

27 requirement can be addressed through the use of diffuse fraction models. In this study, we try to
28 quantify the errors in PV modelling when measurements of the diffuse solar irradiance are not
29 available. For this purpose, we use total and diffuse solar irradiance data obtained from ground-
30 based measurements of BSRN to simulate the PV electric output using GSEE. We have chosen five
31 sites in Europe and North Africa, with different prevailing conditions, where BSRN measurements are
32 available. GSEE incorporates an implementation of the [Boland-Ridley-Lauret \(BRL\)](#) diffuse fraction
33 model, along with a Climate Data Interface that enables simulations across different time scales.
34 We evaluate the capability of BRL in providing accurate estimations of the diffuse fraction under
35 diverse atmospheric conditions, with particular attention on the presence of clouds and aerosols
36 and assess the extent to which its associated errors propagate to energy production modelling.
37 Furthermore, we compare GSEE outputs when using CAMS radiation time-series as input instead of
38 ground-based measurements, to quantify the impact of the CAMS radiation product uncertainties in
39 PV modelling.

40 **Keywords**

41 Solar energy modelling; CAMS radiation; PV power modelling; aerosol; dust; solar radiation

42 **1. Introduction**

43 Decarbonizing the power sector in a sustainable manner is pivotal in the effort to mitigate climate
44 change (Edenhofer et al., 2011; Owusu & Asumadu-Sarkodie, 2016; IPCC, 2023) and the large-scale
45 deployment of Solar Energy offers significant prospects toward this objective (Kakran et al., 2024).
46 The available solar energy is a variable source, fluctuating across different timescales with a unique
47 solar-resource profile over individual locations (McMahan et al., 2013). Therefore, accurate solar
48 energy forecasting and resource assessment is crucial for minimizing the risk in selecting project
49 location, designing the appropriate solar-energy conversion technology, and integrating new sources
50 of solar based power generation into the electricity grid (Stoffel, 2013), while short-term, intra-hour
51 forecasts are critical for power plant operations, grid-balancing, real-time unit dispatching,
52 automatic generation control, and trading (Pedro et al., 2017).

53 [For practical reasons, it is critical to extend Extending](#) solar irradiance forecasting to [encompass](#)
54 [methods linked to solar-based power generation derive](#) PV power forecasts [is essential in solar](#)
55 [energy applications. PV power modelling](#) can be [derivedachieved](#) through the following additional
56 steps to solar irradiance forecasting: (i) decomposing Global Horizontal Irradiance (GHI) into Diffuse

57 Horizontal Irradiance (DHI) and Direct Normal Irradiance (DNI)); (ii) calculating the plane-of-array
58 irradiance incident on the surface of PV planes, whether static or mounted on a solar tracking
59 system, and (iii) simulating the PV power production primarily based on the in-plane irradiance
60 (Blanc et al., 2017).

61 The scarcity of concurrent measurements of both solar irradiance components, coupled with the
62 complexity of their theoretical computation, has driven the development of numerous empirical
63 models for estimating the diffuse fraction (ratio of the diffuse-to-global solar radiation). A seminal
64 contribution in this area was made by Liu and Jordan (1960), who established a correlation between
65 the diffuse fraction and the clearness or cloudiness index (ratio of the global-to-extraterrestrial
66 radiation). These models predominantly rely on the clearness index as the principal predictor. They
67 are generally classified into single-predictor models and multi-predictor models, with the latter
68 incorporating additional astronomical variables for enhanced precision (Paulescu & Blaga, 2019).
69 Typically, these models are expressed as polynomial equations, ranging from the 1st to the 4th degree,
70 that link the diffuse fraction to the clearness index [Jacovides et al., 2006](#): $DF = f(\text{clearness index},$
71 ** params*). [Boland et al., 2001](#) proposed the use of a logistic function
72 instead of linear or simple nonlinear functions of the clearness index. Ridley et al. (2010) developed
73 a multiple-predictor logistic model, known as the Boland-Ridley-Lauret (BRL), which combines
74 simplicity and reliable performance across both the Northern and Southern Hemispheres. [The BRL](#)
75 [model extends Boland's approach by adopting the hourly clearness index as the principal predictor](#)
76 [and introducing the following additional parameters: apparent solar time, daily clearness index, solar](#)
77 [altitude, and a measure of the persistence of global radiation level. In the implementation of the BRL](#)
78 [included in the GSEE, the users set as input only the hourly clearness. Moreover, this implementation](#)
79 [adopts the updated parameters proposed by Lauret et al. \(2013\), which derived using data from nine](#)
80 [worldwide locations covering a variety of climates and environments across Europe, Africa, Australia](#)
81 [and Asia.](#) While the existing models consider all-sky conditions, in solar energy modelling it is critical
82 to focus on cloud-free skies, where energy production is maximized. Under such conditions,
83 aerosols become the primary parameter influencing the distribution of solar irradiance among its
84 components. (e.g., Blaga et al., 2024). [Specifically, the BRL model accounts for aerosols indirectly](#)
85 [through the clearness index, which is indicative of the overall atmospheric attenuation of solar](#)
86 [radiation.](#)

87 [Regions](#)[In regions](#) dominated by abundant sunshine, such as the Mediterranean and Middle East,
88 which are favorable for solar based power generation, the attenuation of solar irradiance is strongly
89 influenced by aerosols, and particularly desert dust aerosols. Several studies highlighted the impact
90 of desert dust aerosol in the downwelling solar irradiance and the energy production in these regions
91 (Fountoulakis et al., 2021; Papachristopoulou et al., 2022);[Kosmopoulos et al., 2018; Kouklaki et](#)
92 [al., 2023](#). The significance of considering the effect of aerosols in short-term solar irradiance
93 forecasting and nowcasting is emphasized by Kazantzidis et al. (2017),[Raptis et al. \(2023\)](#) and
94 Papachristopoulou et al. (2024).

95 The Global Solar Energy Estimator (GSEE; Pfenninger & Staffell, 2016) is a widely used open access
96 model for simulating PV power output, designed for rapid calculations and ease of use;[It](#) comes
97 with an implementation of the BRL diffuse fraction model (Ridley et al., 2010; Lauret et al., 2013).

98 [While PV power modelling is essential for linking solar resources to energy production, the existing](#)
99 [literature does not adequately address its reliability under diverse atmospheric conditions. To the](#)
100 [best of our knowledge, the existing literature does not include studies that explicitly address the](#)
101 [uncertainties in PV energy production modeling associated with the partitioning of solar radiation](#)
102 [into its direct and diffuse components at the model input.](#) In this study, we supply GSEE with input
103 data from ground-based measurements as well as from the Copernicus Atmospheric Monitoring
104 Service (CAMS), aiming to investigate differences in PV power output simulations, which arise from
105 providing only GHI as input radiation data. At the outset, we focus on evaluating the reliability of BRL
106 under diverse atmospheric conditions, with particular attention to the dependence of its accuracy
107 on the presence of clouds and aerosols. To further explore this, we conduct a sensitivity analysis
108 using radiative transfer model (RTM) simulations under cloud-free skies. Following these analyses,
109 we assess the extent to which the associated uncertainties in the estimation of the diffuse fraction
110 spread to the power generation over hourly intervals. This step involves simulating PV plants with
111 varying configurations.

112 GSEE is also effective for analyzing trends and variability in solar based power generation through its
113 climate interface submodule (e.g., Hou et al., 2021);[where the BRL model is integrated within the](#)
114 [internal processing chain](#) The accuracy of the climate interface in estimating the total daily PV power
115 output is also evaluated in this study.

116

117 **2. Data and Methodology**

118 **2.1 Global Solar Energy Estimator (GSEE)**

119 The modelling of the PV power output is conducted using the version 0.3.1 of GSEE (Pfenninger &
120 Staffell, 2016). The model features functions for simulating a complete PV system, incorporating
121 characteristics and specifications such as location, installed capacity, technology, tracking (fixed, 1-
122 axis, 2-axis), tilt angle, and orientation.

123 The user provides as input time-series data of solar radiation, and optionally, ambient air
124 temperature and surface albedo. Specifically, the model requires GHI and, when available, the
125 Diffuse Fraction. If the diffuse component is not provided, the provided implementation of the BRL
126 diffuse fraction model (Ridley et al., 2010; Lauret et al., 2013) is employed to estimate it, relying only
127 on time-series of the hourly clearness index and the geographical coordinates. [While in the single-](#)
[site application of the GSEE model with hourly time resolution the user has the option to adjust the](#)
[input and select alternative diffuse fraction models implemented by external libraries, e.g., pvlib](#)
[\(Anderson et al., 2013\), the climate data interface automatically invokes the BRL model as part of the](#)
[internal processing workflow.](#) GSEE utilizes the provided information for the distribution of the
132 irradiance components and applies trigonometric calculations to determine the total solar
133 irradiance incident on the panel's inclined plane. [More precisely, for the plane-of -array irradiance](#)
[calculation a GSEE includes the submodule "trigon" \(transposition model\), which is based on](#)
[trigonometric formulations, that account of the surface albedo, thereby including the ground-](#)
[reflected component of solar radiation. However, the transposition model is integrated within the](#)
[GSEE internal algorithms, so it cannot be modified by the user.](#)

138 After solar irradiance the most significant parameter regarding energy production is [air](#) temperature
139 (e.g., Dubey et al., 2013). If temperature is not provided by the user, the model assumes a default
140 value of 20 °C. In this study, temperature was used as input only in the simulations with BSRN data,
141 as it is provided alongside [actinometricradiation](#) measurements. A surface albedo value of 0.3
142 considered by default from the model, introduces some uncertainty in our simulations-[, which](#)
[however is estimated to be small. Under cloudless conditions, a 10% difference in surface albedo](#)
[changes the GHI by ~1% for SZA < 75°. Differences are larger under cloudy conditions \(~ 10%](#)
[difference in GHI for a 10% difference in surface albedo\).](#) Nevertheless, surface albedo at the
146 selected sites is generally low and relatively invariant throughout the year (even at the most northern

147 site of Lindenberg there is only a limited number of days with increased surface albedo due to snow
148 cover).

149 The available options for the panel type are crystalline silicon (c-Si) and Cadmium Telluride (CdTe),
150 where the power output is modeled based on the relative PV performance model described by Huld
151 et al. (2010). For fixed panels, a built-in latitude dependent function for the optimal tilt is also
152 included.

153 Moreover, GSEE includes a Climate Data Interface submodule that enables the processing of gridded
154 climate datasets, with varying temporal resolutions, ranging from hourly to annual. Within the
155 context of this submodule, the use of BRL serves as part of the resampling and upsampling
156 processes applied to input climate datasets with daily resolution. For processing data with lower-
157 than-daily resolutions, it incorporates the use of Probability Density Functions (PDFs), which
158 describe the probability with which a day with a certain amount of radiation occurs within a month
159 (Renewables Ninja, n.d.). This methodology accounts for the non-linear distribution of mean monthly
160 radiation across individual days, ensuring a more representative temporal disaggregation. The
161 processes applied to the mean daily irradiance are described in detail in Section 3.4.

162 For the purposes of this study, we simulated solar plants with capacity of 1 kWp, and for both
163 available technologies. The simulations with c-Si technology, considered as default by the model,
164 are presented ~~detailed~~ in detail the following sections. The results of the simulations with CdTe
165 technology are provided in the supplement, and are not thoroughly discussed, since they are very
166 similar to the results for the c-Si technology. Regarding the mounting approach, the solar plants were
167 either static and oriented to the south or equipped with a 2-axis solar tracking system. In the case of
168 fixed panels, we selected the optimal tilt angle relying on the latitude dependent built-in function.

169 The input parameters defining the characteristics of the simulated PV plants are summarized in Table
170 1.

171 **Table 1.** Input parameters defining the characteristics of the simulated PV plants

Capacity	Mounting Approach		Technology	
1 kWp	Fixed	2-axis tracking	c-Si	CdTe

	Orientation: south	Tilt Angle: $f(\text{latitude})$ built-in function for optimal tilt			
--	-----------------------	---	--	--	--

172

173 **2.2 Ground-based measurements**

174 We supplied GSEE with ground-based irradiance as well as ambient temperature measurements
 175 collected from five stations of the Baseline Surface Radiation Network (BSRN; Driemel et al., 2018).
 176 Moreover, information about aerosols was retrieved from co-located stations of the Aerosol Robotic
 177 Network (AERONET; Holben et al., 1998; Dubovik et al., 2000).

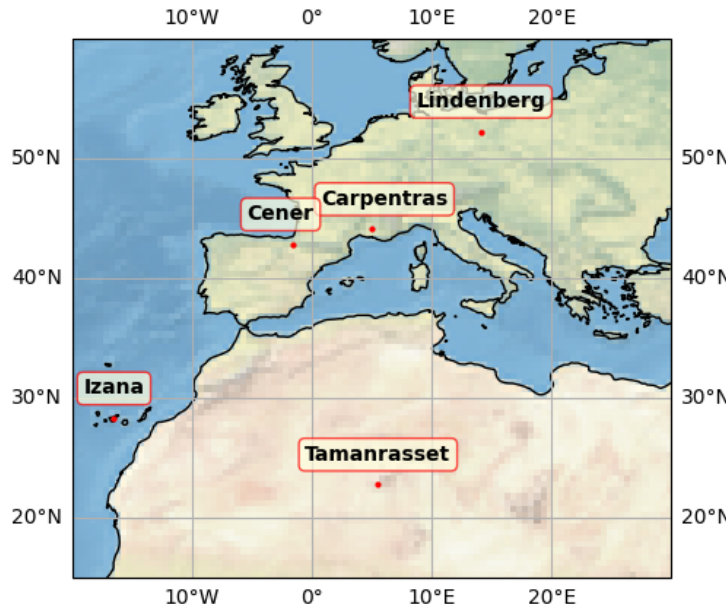
178 Information for the stations utilized for this study is summarized in Table 2, and their geographical
 179 location is depicted in Figure 1.

180

181 **Table 2.** Detailed information about the location of the ground-based stations used in this study.

STATION	Latitude [° N]	Longitude [° E]	Elevation [m]
Carpentras (CAR)	44.08	5.06	100
Cener (CNR)	42.82	-1.60	471
Izaña (IZA)	28.31	-16.50	2373
Lindenberg (LIN)	52.21	14.12	125
Tamanrasset (TAM)	22.79	5.53	1385

182



183

184 **Figure 1.** Locations of the BSRN and co-located AERONET stations that are used in the current
185 study

186

187 BSRN station-to-archive files were accessed and manipulated using the SolarData v1.1 R package
188 (Yang, 2019), and the BSRN-recommended quality check (QC) tests (Long & Dutton, 2010) applied
189 to the collected data. Some data gaps arose due to measurements removed during the QC
190 procedure. Although these data gaps are, in most cases, shorter than 2-3 hours, they may affect the
191 BRL performance throughout the corresponding days. Consequently, days affected by such data
192 gaps excluded from the analysis. We retrieved data for 2017, with 1-minute temporal resolution. We
193 used GHI, DHI, and Temperature as inputs to the GSEE model. Initially, the data were resampled to
194 hourly, and mean hourly values of GHI and DHI are calculated. Then, the simulations were
195 conducted using either GHI and DHI, or only GHI along with the deployment of BRL. The input to BRL
196 consists of hourly clearness index, derived by dividing GHI measurements with the solar radiation

Formatted: Font color: Text 1

197 incident on a horizontal plane at the Top of the Atmosphere (TOA) above the examined location.
198 Subsequently, the 1-min timeseries resampled also to a daily resolution and transformed into three-
199 dimensional arrays, $GHI = f(\text{time}, \text{lat}, \text{lon})$, where the spatial dimensions of each dataset
200 corresponded to a unique point defined by the coordinates of the associated station. Simulations
201 with the daily time-resolved dataset were performed using the Climate Data Interface.

202 [Measurements](#)[Representing cloudiness is a challenging task that requires several observations. For](#)
203 [this purpose, aiming to obtain an indicative measure of the intra-hour cloudiness conditions we](#)
204 [adopted the following formulation. Specifically, measurements](#) of Direct Normal Irradiance (DNI)
205 were utilized to obtain information for cloudiness relying on the conditions stated by WMO (2021),
206 according to which sunshine duration is the total period where DNI exceeds 120 W/m^2 . [Alternative](#)
207 [approaches such as the Cloud Modification Factor, require estimates of the clear sky irradiance,](#)
208 [which introduces additional uncertainty.](#) For the purpose of this analysis, we introduced a solar
209 visibility (SV) parameter. Specifically, we assigned the value 0 when sun was obscured and the value
210 1 when visible. Aiming to describe the mean intra-hour cloudiness conditions, we considered the
211 sky as cloud-free, cloudy, and partly cloudy based on the mean SV for the entire corresponding hour
212 as follows:

$$\langle SV \rangle_{\text{hour}} : \begin{cases} 1 & \text{cloud-free} \\ \in (0,1) & \text{partly cloudy} \\ 0 & \text{cloudy} \end{cases}$$

213 For aerosol information, we accessed the AERONET Version 3 (V3) (Giles et al., 2019) and retrieved
214 level 2.0 data (from direct sun measurements) for Aerosol Optical Depth at 500nm (AOD_{500}), which
215 serves as a representative measure of the aerosol load; Ångström Exponent between 440 and 870
216 nm wavelengths ($AE_{440-870}$), where values near 0 correspond to coarse dust particles and values
217 around 2 to fine (e.g., smoke) particles (Dubovik et al., 2002); and Fine Mode Fraction at 500nm
218 (FMF_{500}) obtained from the Spectral Deconvolution Algorithm (SDA) retrievals, to distinguish aerosol
219 into fine and coarse mode. The data were resampled at hourly intervals and [a mean hourly value](#)
220 [calculated. After, the hourly mean values](#) divided into clusters [regarding AOD based on AOD₅₀₀](#),
221 reflecting different levels of aerosol load and allowing us to quantify their impact on solar energy
222 production. To investigate the impact related exclusively to aerosols, we included only hours with
223 cloud-free sky conditions. The clusters are defined in detail as follows:

225 • $AOD_{500} \leq 0.05$: Low aerosol load

226 • $0.05 < AOD_{500} \leq 0.15$: Moderate aerosol load
227 • $0.15 < AOD_{500} \leq 0.3$: High aerosol load
228 • $AOD_{500} > 0.3$: Very high aerosol load

229 To evaluate the performance of the Climate Interface over daily intervals, we defined the sunny
230 (cloudless) days using the condition: $\langle SV \rangle_{day} \geq 0.9$. Next, to characterize the average aerosol
231 conditions on sunny days, we applied the following classification:

232 • $\langle AOD_{500} \rangle_{day} \leq 0.05$: very-low aerosol
233 • $\langle AOD_{500} \rangle_{day} > 0.05$: aerosol-laden

234 Detailed comparisons of the energy production over hourly and daily integrals^c under the various
235 predefined sky conditions are provided in the supplement through evaluation metrics.

236 The selected locations have quite different atmospheric conditions regarding cloudiness and
237 aerosols. Additionally, they vary in altitude. A brief overview of the prevailing conditions derived from
238 the ground-based data is provided on the supplement. Regarding cloudiness, it is notable that in
239 Lindenberg the sky is generally overcast, whereas in southern locations sunshine dominates. In
240 terms of aerosols, very high aerosol loads occur more frequently in Tamanrasset. As for aerosol type,
241 there is considerable variation among the examined locations: Carpentras, Cener, and Lindenberg
242 are primarily influenced by fine mode aerosols, while Tamanrasset and Izaña are mostly affected by
243 coarse mode aerosols.

244 For investigating the impact of desert dust aerosol in solar based power generation, Tamanrasset
245 serves as a representative and exceptional case because it is in a region with important sources of
246 Saharan dust aerosols (Faid et al., 2012). Meanwhile, Izaña, located in subtropical North Atlantic, is
247 a high mountain station within the free troposphere, affected^{my} mineral dust when the Saharan Air
248 Layer top exceeds the station height, especially through August to October (Toledano et al., 2018;
249 Cuevas et al., 2018). Due to its high altitude, Izaña avoids contamination from local or regional
250 sources (Barreto et al. 2022). The Canary Islands, where Izaña is located, are influenced by extreme
251 dust events that cause a significant decrease in PV power generation (Canadillas-Ramallo et al.,
252 2021). In South Europe, which is also affected by the transport of Saharan dust across the
253 Mediterranean, aerosol types exhibit a mixture as a result of simultaneous local pollution and low
254 concentration of mineral dust (Logothetis et al., 2020).

255 2.3 Copernicus Atmospheric Monitoring Service (CAMS)

256 We retrieved data from the CAMS radiation service (Schroedter-Homscheidt et al., 2022; Qu et al.,
257 2017), from the solar radiation time-series product (CAMS, 2020). The CAMS solar radiation service
258 provides historical estimates for global solar radiation, along with its components, from 2004 to
259 present. These values are provided with a frequency as fine as 1-minute. In this study, we used the
260 hourly time-series of GHI and DHI for all-sky conditions, setting the input coordinates to match the
261 locations of the BSRN stations. [The solar radiation time-series product \(CAMS, 2020\) performs
interpolations integrated in its internal algorithm and provides time-series for the coordinates and
the altitude of a single-site location.](#) We compared the solar energy production derived from the use
262 of CAMS data with that derived from the use of ground-based measurements from BSRN.
263

264

265 2.4 Radiative Transfer Model (RTM)

266 We performed Radiative Transfer (RT) simulations aiming to further assess the uncertainties in
267 estimating the diffuse fraction arising from the effect of aerosols. The simulations were conducted
268 using libRadtran (Emde et al., 2016; Mayer & Kylling, 2005), a widely used software package, allowing
269 the computation of radiances, irradiances, and actinic fluxes. A sensitivity analysis was performed
270 by comparing the diffuse irradiance calculated from libRadtran with the estimations of BRL. This
271 analysis examines the dependence of the aerosol-related discrepancy as function of Solar Zenith
272 Angle (SZA) and latitude, considering the effect of parameters such as surface albedo and altitude.
273 To conduct aerosol parameterizations, we considered the default aerosol extinction profile (Shettle,
274 1989) and set asymmetry factor (gg) to 0.7, while varying the Single Scattering Albedo (SSA) and the
275 Ångström Exponent (AE), and defining AOD_{500} by adjusting the value of the parameter-b in
276 Ångström's law (Ångström, 1929) as follows:

$$\tau_\lambda = b \cdot \lambda^{-a} \rightarrow AOD_{500} = b \cdot (0.5 \mu m)^{-AE}$$

277

278 The standard aerosol profiles (Anderson et al., 1986) were used for all sites. According to
279 Fountoulakis et al. (2022), using a more accurate vertical distribution of aerosols in the troposphere
280 would have a negligible effect in the GHI and DHI at the Earth's surface.

281 Table 3 illustrates the libRadtran settings used in this study.

282 **Table 3.** LibRadtran inputs

Parameter	Input
Atmospheric profile	Mid-latitude summer (April-September)/mid-latitude winter (October - March) (Anderson et al., 1986)
Extraterrestrial spectrum	(Kato et al. 1999)
<u>SZA</u> <u>Datetime</u>	<u>with step 90° date and time input accompanied by project location coordinates</u>
Altitude	0.1/2 km
Surface albedo	0.2 / 0.8
Number of streams	6
RT solver	sdisort (Buras et al., 2011)
AE	0 – 2 with step 1
SSA	0.7, 0.9, 1.0
gg	0.7
TOC (Total Ozone Column)	300 DU
<u>Integrated</u> Water <u>vapor</u> <u>Vapor</u>	15 mm

283

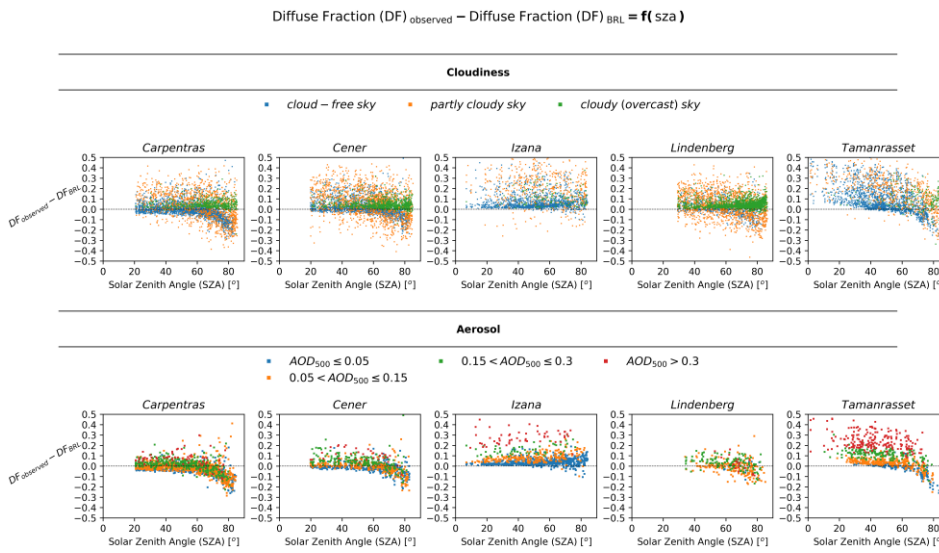
284 **3. Results**

285 **3.1 Performance verification of the BRL diffuse fraction model**

286 The performance of BRL was evaluated by comparing the actual diffuse fraction, obtained directly
 287 from resampled to hourly BSRN ground-based measurements, with that derived using BRL.
 288 InitiallyAs a first step, to isolate the influence of SZA from that associated with the atmospheric
 289 conditions, the difference in diffuse fraction (DF) between the observed and the one estimated using
 290 BRL as a function of SZA is presented in Figure 2. The atmospheric conditions are represented
 291 separately for both all-sky and cloud-free sky conditions and are grouped into clusters, as outlined
 292 in Section 2.2. The patterns reflecting the differences under the distinct sky conditions indicate an
 293 additional dependency on SZA, which becomes apparent approximately beyond 60° at SZA between
 294 60° and 70°. In most cases, there is an almost constant displacement with respect to y=0 below 60°,

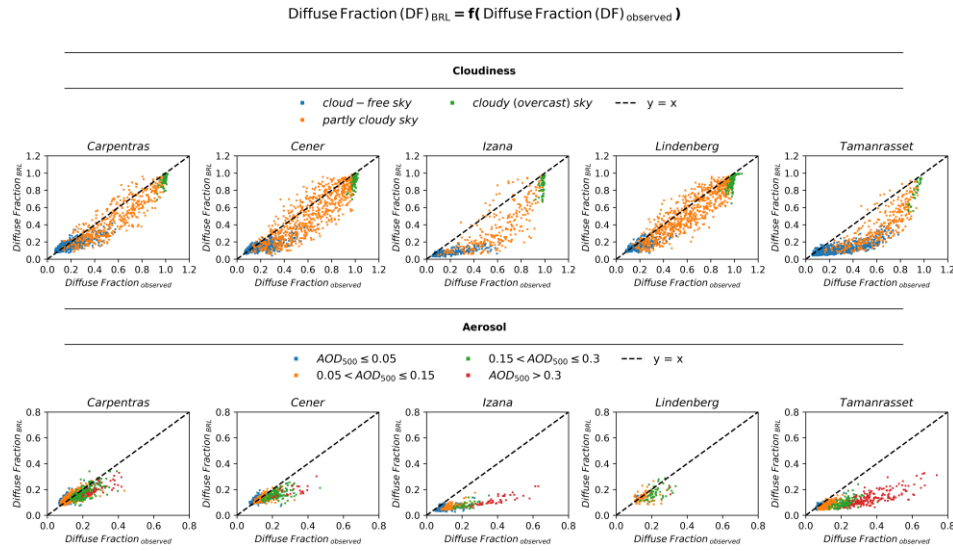
295 as well as a negative trend change in behavior when SZA exceeds this value. Izaña presents a special
 296 case, as the station is located at a very high altitude, with adjacent clouds occasionally being
 297 situated at a. At such high altitudes the contribution of the diffuse component to the total irradiance
 298 is significantly smaller relative to lower elevation than the station itself. As a result altitude sites,
 299 which seems to be captured more accurately by BRL at high SZAs. We must also note that (i) at Izaña,
 300 the actual diffuse irradiance experiences may experience an additional enhancement due to the
 301 contribution of these adjacent lower-lying clouds – an effect that is not accounted for in the diffuse
 302 fraction model, and (ii) during dust events the site is usually inside – and not under – the dust layer,
 303 which results in more complex interactions between dust and solar radiation relative to lower
 304 altitude sites. Defining an exact limit (for the lower altitude sites), where the behavior is changing, is
 305 challenging; therefore, 60° was selected for practical energy-related applications, focusing on
 306 periods with meaningful energy contribution, and is supported by the sensitivity analysis (Section
 307 3.2) under clear-sky conditions. Concerning the same grouped atmospheric conditions, Figure 3
 308 illustrates the comparison between the observed and the estimated diffuse fraction for $SZA \leq 60^\circ$.
 309 This approach allows us to examine BRL performance after eliminating the influence of SZA, thereby
 310 providing a more comprehensive view of its reliability.

Formatted: English (United Kingdom)



311
 312 **Figure 2.** Difference between the observed and the diffuse fraction estimated by the ground-based
 313 measurements and by using the BRL diffuse fraction model as a function of SZA under diverse

314 atmospheric conditions: (top) classification with respect to cloudiness and (bottom) classification
 315 with respect to aerosol optical depth



316

317 **Figure 3.** Comparison of the diffuse fraction estimated using BRL with the actual one calculated
 318 directly from that estimated by the ground-based measurements under diverse atmospheric
 319 conditions for SZA < 60°: (top) classification with respect to cloudiness and (bottom) classification
 320 with respect to aerosol optical depth

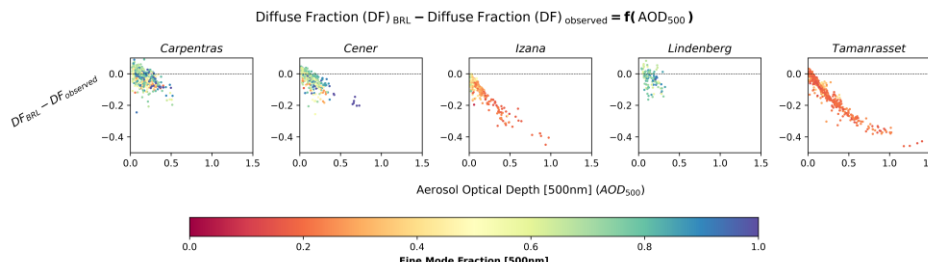
321

322 From Figure 3, a distinct dependency of BRL's reliability on the atmospheric conditions can be
 323 observed. Under all-sky conditions, the presence of clouds has a notable impact on the
 324 model's performance. Partly cloudy conditions result in greater dispersion of the values from
 325 the identity line respectively, likely due to the complexity of such sky scenes. Under overcast
 326 conditions, where the sky can be considered homogeneous and isotropic, the model performs
 327 slightly better. However, the limitations of the DNI-based
 328 classification methodology, related to the complexity of the cloud scenes, the spatiotemporal
 329 variability during the hourly periods, and the 3D variability of cloud properties, would require
 330 additional observational tools for a more detailed investigation. More specifically, the vast majority
 331 of overcast cases where the BRL diffuse fraction is below 0.8 while the observed is close to 1

332 correspond to periods involving rapid transitions between partly cloudy and overcast skies, occurring
333 either during the hour itself or immediately before or after it. Furthermore, a limited number of cases
334 identified during intense dust events at Tamanrasset and Izana, where the reduction of DNI was so
335 pronounced that the applied DNI-based criterion classified these conditions as overcast. However,
336 these cases are not further investigated, as the energy production levels during such periods are very
337 low.

338 Under cloud-free skies, BRL tends to underestimate, and this bias becomes more pronounced as
339 aerosol load increases. Aiming to highlight this dependency, Figure 4 shows the difference between
340 the estimated and the observed diffuse fraction as function of AOD_{500} , emphasizing also the extent
341 to which it is related to the aerosol type by providing FMF_{500} . A negative trendA decrease for
342 increasing AOD_{500} is evident across all cases. In Tamanrasset and Izaña, associated with the
343 influence of Saharan dust, the coarse mode dominates, and a more distinct and well-defined curve
344 is depicted- compared to other sites.

345 It is important to clarify that for assessing the impact of aerosols we have assumed entirely cloud-
346 free conditions. However, the criterion applied based on DNI does not fully guarantee the absence of
347 small, scattered clouds within the sky dome. Such clouds could induce slight enhancements in DHI.
348 A more rigorous assessment of the impact associated exclusively with aerosols could be achieved
349 by integrating images from ground-based co-located all-sky cameras. On the other hand, the
350 presence of aerosols even under cloudy scenes, introduces an additional uncertainty which is
351 difficult to investigate accurately.



352
353 **Figure 4.** Difference between the estimated using BRL and actual diffuse fraction
354 estimated by the ground-based measurements as function of AOD_{500} and FMF_{500}

356 [3.2 Sensitivity analysis of the BRL performance under cloud-free sky conditions from RT](#)
357 [simulations](#)

358 The uncertainties in estimating diffuse fraction under cloud-free sky conditions, as discussed in
359 section 3.1, are further investigated. We performed RT simulations using libRadtran to calculate GHI
360 and DHI under various aerosol scenarios. The resulting GHI values were then used as input to BRL to
361 estimate the diffuse fraction, which was subsequently compared to the diffuse fraction derived
362 directly from the ratio of DHI to GHI computed by libRadtran.

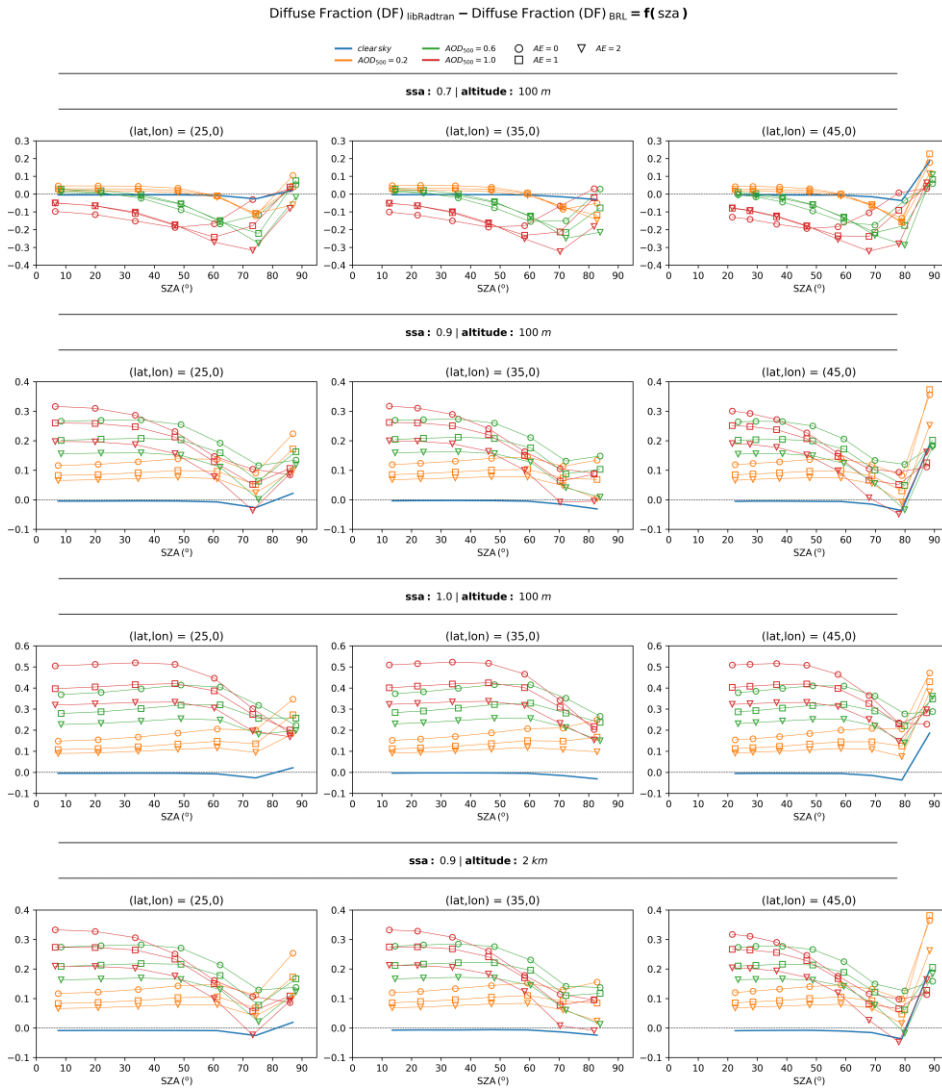
363 To ensure a comprehensive analysis, we considered three representative latitudes (25°, 35° and 45°).
364 Since BRL requires an hourly time-series of GHI as input, the analysis was conducted for the summer
365 solstice. On this day, a sufficient number of hourly values are available, corresponding to a wide
366 range of SZA values, allowing for a robust assessment of the methodology. The sensitivity analysis
367 was performed for surface albedo values of 0.2 and 0.8 as well as for altitudes of 0, 1 and 2 km. For
368 aerosol parameterization, we examined completely clear-sky conditions as a reference, alongside
369 scenarios with AOD_{500} values of 0.2, 0.6, and 1, while varying the SSA and AE. Specifically, the
370 scenarios included SSA values of 0.7, 0.9 and 1, combined with AE values of 0, 1 and 2. The results
371 of this sensitivity analysis for an albedo of 0.2 are provided in Figure 5, while the results for an albedo
372 of 0.8 are included in the supplement (Figure S1).

373 The results confirm that BRL performs well under clear sky conditions and for SZA below 60°, while
374 the incorporation of aerosols in the sky scene introduces larger uncertainties. In all scenarios, we
375 observe that lower values of AE correspond to higher uncertainties. Moreover, [regarding SSA](#), when
376 SSA is 0.9 or 1 BRL gradually tends to underestimate the diffuse fraction as aerosol load increases.
377 Instead, when SSA is 0.7, BRL exhibits a different behavior, shifting toward an overestimation of the
378 diffuse fraction at high aerosol loads.

379 The findings of this sensitivity analysis are consistent with the evaluated BRL performance from
380 ground-based measurements presented in section 3.1, [especially at SZA smaller than 60° - 70°](#), and
381 underscore the role of aerosol in the accuracy of diffuse fraction estimations. [Differences between](#)
382 [the results shown in Figures 2 and 5 at SZA between 60° - 80° can be due to a number of site-related](#)
383 [reasons. For example, enhancement of the diffuse component due to scattering by underlying](#)
384 [atmospheric layers and clouds in the case of Izaña may compensate the observed overestimation of](#)
385 [the diffuse fraction by BRL](#). Concerning the impact related to AE and SSA, we confirm that the higher

386 underestimations observed for Tamanrasset and Izaña are associated with the optical properties of
387 desert dust aerosol particles. While AE and SSA alone are not sufficient to fully characterize the
388 aerosol type, they serve as strong indicators, aligning with the classification framework of Dubovik et
389 al. (2002). The same comparison for albedo 0.8 (Figure S1 in the supplement) reveals a significant
390 broadening of the discrepancies. Moreover, we observe the presence of a systematic error, even
391 under clear sky conditions.

392 *The resulting differences were practically identical across the three selected latitudes, indicating*
393 *that the BRL model is largely independent of latitude and can therefore be considered as a reliable*
394 *solution over a wide range of latitudes. Furthermore, the effect of altitude was found to be small.*
395 *Finally, the outcomes of this analysis highlight potential inconsistencies arising from aerosols with*
396 *different optical properties. Although the updated parameters of the BRL's model (as implemented*
397 *in the GSEE model) reported by Lauret et al. (2013) were derived using data from nine worldwide*
398 *locations, encompassing a broad range of sky conditions that capture a fully representative set of*
399 *optical properties remain challenging.*



401 **Figure 5.** Difference between the diffuse fraction derived directly from the computations of DHI and
 402 GHI using libRadtran and the one estimated by applying BRL to the libRadtran-computed GHI

403

404

405 3.3 Analysis of the differences in energy production using hourly integrals within the modelling of PV
406 plants

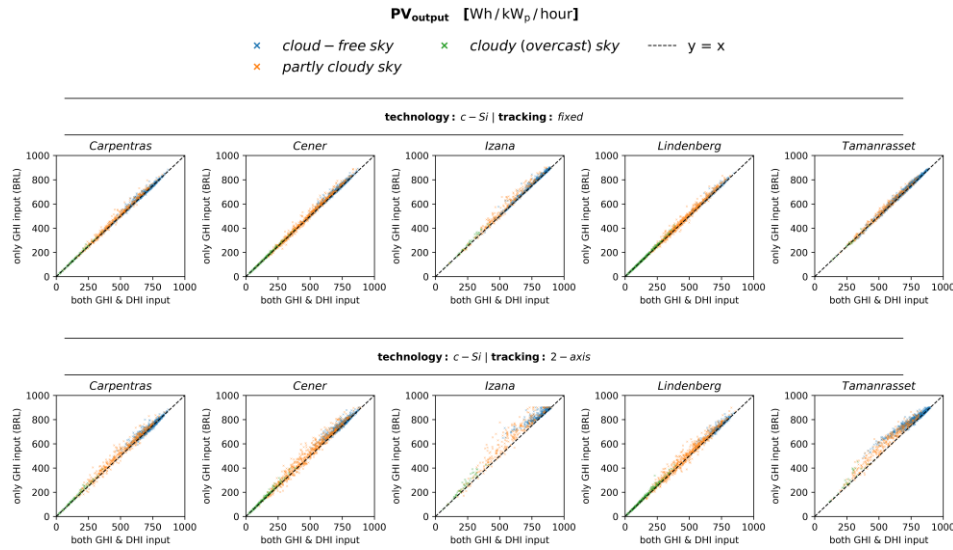
407 Uncertainties in estimating the diffuse fraction influence the calculation of the total irradiance
408 received by an inclined panel's surface, thereby affecting the accuracy of the PV power simulations.
409 In this section, we employ the main submodule of GSEE, used for modelling the electric output from
410 a PV panel, aiming to assess the extent to which these uncertainties propagate to the estimation of
411 the hourly power production. We analyze discrepancies arising from using only GHI from BSRN as
412 input radiation data to the model, instead of both DHI and GHI. More specifically, we compare the
413 total energy produced per hour per unit, expressed in watt-hours (Wh), per unit of nominal power
414 (kWp). The energy production is evaluated for both fixed panels and 2-axis tracking systems.

415 The results of this comparison for c-Si based technology PV panels for different atmospheric
416 conditions are presented in Figure 6, illustrating the impact of cloudiness, and in Figure 7,
417 demonstrating the effect of aerosols. The corresponding results for CdTe technology are provided in
418 the supplement (Figures S2 and S3 respectively). In the modelling of 2-axis solar tracking systems,
419 where the panel is continuously adjusted to maintain a perpendicular orientation to incoming solar
420 radiation, the system becomes more sensitive to uncertainties in the estimation of the diffuse
421 fraction, leading to more significant differences in energy production. Specifically, the contribution
422 of the direct irradiance is maximized in such systems, as the panel exploits the entirety of the
423 available direct irradiance. On the other hand, in the simulation of static panels, the contributions of
424 direct and diffuse components are more evenly distributed, making the impact of diffuse fraction
425 uncertainties less pronounced in energy production.

426 Regarding the uncertainties related to the atmospheric conditions, from Figure 6 we confirm that the
427 highest dispersion occurs in partly cloudy conditions, while from Figure 7, where we examine cloud-
428 free conditions, we note that further improvement achieved as aerosol load decreases. Under totally
429 overcast skies the energy production is extremely low, rendering errors practically negligible.
430 Moreover, accuracy is influenced by aerosols, where a gradual decline in accuracy is detected as
431 aerosol load increases. However, assessing the extent of aerosol loading impact is complex,
432 depending on the interaction of solar radiation with particles of varying optical properties, as
433 extensively analyzed in the previous sections. This effect becomes particularly evident in cases of
434 high aerosol loading, where a noticeable offset is observed, while under certain conditions, the
435 associated uncertainty is comparable to that found in partly cloudy conditions.

436

437 **Figure 6.** Comparison of the estimated hourly PV power generation between simulations performed
 438 using GSEE with input data consisting of either only GHI or both GHI and DHI under varying
 439 cloudiness conditions: (top) fixed panels (bottom) 2-axis tracking systems



440

441 **Figure 7.** Comparison of the estimated hourly PV power generation between simulations performed
 442 using GSEE with input data consisting of either only GHI or both GHI and DHI under varying aerosol
 443 conditions: (top) fixed panels (bottom) 2-axis tracking systems

444 The PV systems considered in this study have a nominal capacity of 1 kWp. The PV model applies a
 445 default system loss factor of 10%. This effectively limits the maximum achievable power output to
 446 approximately 90% of the nominal capacity (i.e., around 900 W/kWp). This effect becomes apparent
 447 at the Izaña site due to its low latitude combined with its specific geographical and atmospheric
 448 conditions, which lead to high irradiance levels. As a result, the simulated PV output in some cases
 449 appears capped around 900 Wh/kWp per hour when only GHI is used.

450 Additionally, Tables S1-S5 in the supplement,4 and 5 present the validation results, including
 451 computed for Carpentras and Tamanrasset, selected as representative locations that encompass a
 452 wide variety of sky conditions. Validation results for the remaining stations are available in the
 453 supplement (Tables S1-S3). All the evaluation metrics that quantify the errors. All the computations
 454 correspond to simulations of PV panels with c-Si technology.

455 **Table 4.** Evaluation metrics for GSEE performance within hourly intervals in Carpentras, comparing
 456 simulations with diffuse fraction from measurements and from the BRL model

STATION: Carpentras		fixed panels			2-axis tracking		
		RMSE (Wh/kWp/hour)	MAE (Wh/kWp/hour)	rMBE (%)	RMSE (Wh/kWp/hour)	MAE (Wh/kWp/hour)	rMBE (%)
All-Sky scenes		12.6	6.6	0.8	20.8	12.5	1.2
All-Sky scenes (cloudiness)	cloud-free	9.2	4.6	0.4	14.8	8.7	0.5
	partly cloudy	19.5	12.5	2.3	32.5	23.9	3.8
	cloudy (overcast)	5.8	3.0	2.0	10.5	6.1	4.6
Cloudless- Sky scenes (aerosol load)	low	4.7	3.4	-0.4	9.5	7.5	-0.8
	moderate	4.3	2.2	0.1	7.8	4.7	0.0
	high	6.4	4.0	0.6	11.0	7.8	0.9
	very high	14.9	10.2	1.6	22.7	17.2	2.6

457

458 **Table 5.** Evaluation metrics for GSEE performance within hourly intervals in Tamanrasset,
 459 comparing simulations with diffuse fraction from measurements and from the BRL model.

STATION: Tamanrasset		fixed panels			2-axis tracking		
		RMSE (Wh/kWp/hour)	MAE (Wh/kWp/hour)	rMBE (%)	RMSE (Wh/kWp/hour)	MAE (Wh/kWp/hour)	rMBE (%)

All-Sky scenes		13.6	9.3	1.0	40.4	27.8	3.8
All-Sky scenes (cloudiness)	cloud-free	11.5	8.0	0.8	35.3	23.4	2.9
	partly cloudy	20.1	15.0	2.0	56.1	45.7	8.1
	cloudy (overcast)	8.4	5.2	-0.1	45.3	30.1	11.2
Cloudless-Sky scenes (aerosol load)	low	3.2	2.0	0.2	6.6	4.0	0.3
	moderate	5.4	4.6	0.6	13.0	10.5	1.2
	high	12.5	11.7	1.6	30.1	27.4	3.4
	very high	18.0	16.2	1.9	57.0	49.2	6.8

460

461 Based on the calculated statistical indices, the Root Mean Square Error (RMSE) values for fixed
 462 panels range from 4.7 Wh/kWp/hour (clear sky) to 19.5 Wh/kWp/hour (partly cloudy) in Carpentras,
 463 and from 3.2 to 20.1 Wh/kWp/hour in Tamanrasset. Under very high aerosol loading, RMSE reaches
 464 14.9 and 18.0 Wh/kWp/hour, respectively. For 2-axis tracking systems, RMSE values vary
 465 significantly, ranging from 9.5 to 32.5 Wh/kWp/hour in Carpentras and from 6.6 to 56.1 Wh/kWp/hour
 466 in Tamanrasset, with peaks of 22.7 and 57.0 Wh/kWp/hour under very high aerosol loading
 467 conditions. Similarly, the Mean Absolut Error (MAE) values are generally lower for fixed panels (3.4-
 468 12.5 Wh/kWp/hour in Carpentras, 2.0-15.0 in Tamanrasset) and substantially higher for 2-axis
 469 tracking (7.5-23.9 and 4.0-45.7 Wh/kWp/hour, respectively). Notably in Tamanrasset, MAE values
 470 under very high aerosol loading exceed those observed under partly cloudy conditions, with values
 471 increasing from 15.0 to 16.2 Wh/kWp/hour for fixed panels and from 45.7 to 49.2 Wh/kWp/hour for
 472 2-axis tracking systems. Regarding the relative mean bias (rMBE), this remains mostly within $\pm 4.6\%$
 473 for fixed panels but can reach up to 11.2% for 2-axis tracking, particularly in aerosol-laden
 474 conditions.

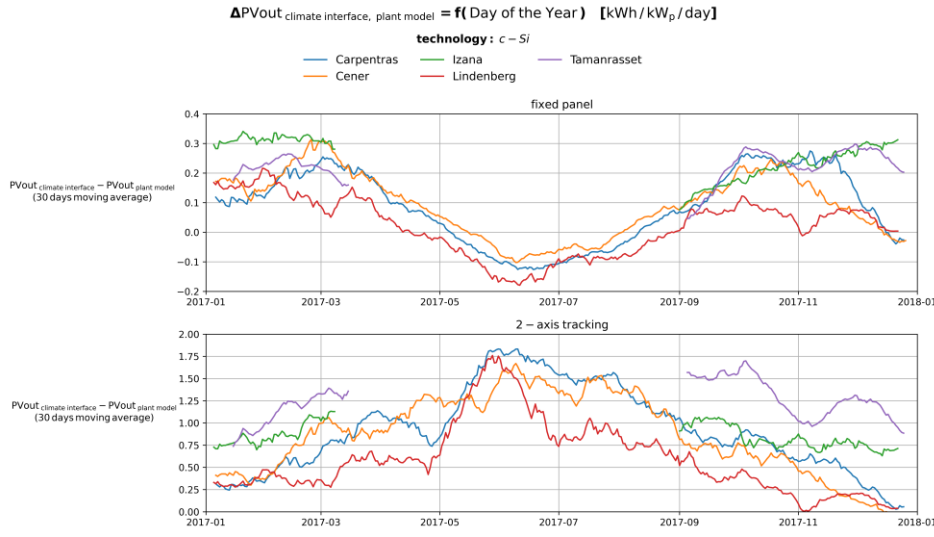
475

476 3.4 Estimating total daily PV power output using the Climate Interface

477 Validation of the estimated daily energy production using the Climate Interface is achieved by
 478 comparing the estimates with the results obtained from the direct summation of the hourly
 479 simulations with input both GHI and DHI.

480 The Climate Interface generates the hourly profile of GHI for each day as a sinusoidal function. Then,
 481 the BRL is applied to the hourly time-series, and the hourly power generation is computed. Finally,
 482 these values are summed up to provide an estimate of the total daily output power. As shown in
 483 Figure Fig. 8, which illustrates the differences between the Climate Interface estimates and the sums

484 of the hourly simulations, this approach introduces a variability throughout the year. [Furthermore](#),
 485 [Figure S6 in the supplement presents the percentage differences between the two approaches, using](#)
 486 [the latter as the reference](#).



487
 488 **Figure 8.** Time-series of the differences between the daily PV output estimated using the climate
 489 interface and the corresponding daily sums from hourly simulations.
 490

491 The time-series represent the [centered](#) 30-day moving average. To ensure that the values are
 492 representative of the reference period, we have applied all conditions requiring at least 20 days of
 493 available data within each 30-days interval. In Tamanrasset and Izaña, especially during the summer
 494 months, there are significant data gaps on several days, often occurring around solar noon.

495 More precisely, from [Figure Fig. 8](#), we observe that within the modelling of PV plants with fixed panels,
 496 there is a tendency to overestimate in winter, with deviations of approximately 0.3 kWh/kWp/day, and
 497 to slightly underestimate in summer, where deviations are around 0.1 kWh/kWp/day. In contrast, for
 498 2-axis solar tracking systems, the resulting deviations are significantly larger, with a general tendency
 499 toward overestimation that peaks during summer, reaching approximately 1.75 kWh/kWp/day. [The](#)

500 percentage differences span from -10 to 20 % for fixed panels and from -5 to 35 % for 2-axis tracking
501 systems.

502 The variability in the percentage difference between the daily PV output estimated using the climate
503 interface and the corresponding daily sums is mainly a function of the minimum SZA, while
504 especially in the case of modeling for 2-axis tracking systems, the variation is also influenced by
505 aerosol loading, with differences tending to increase as aerosol load rises (Figures S4 and S5 in the
506 supplement).

507 Additional validation results are provided in the supplement (Tables S6-S10). Indicatively, for
508 Carpentras and Tamanrasset, representative results are discussed below. For fixed panels, RMSE is
509 minimized at 0.18 kWh/kWp/day under very-low aerosol conditions, compared to the overall 0.22
510 kWh/kWp/day for Carpentras. In Tamanrasset, the lowest RMSE is observed at 0.15 kWh/kWp/day
511 under very low aerosol conditions, while the overall reaches 0.24. In the case of 2-axis tracking, a
512 significant increase is observed from low-aerosol to aerosol-laden conditions, ranging from 0.82 to
513 1.28 kWh/kWp/day in Carpentras and from 0.66 to 1.37 in Tamanrasset. Similar widening trends are
514 also evident in the MAE values across different aerosol loading conditions. The computed statistical
515 indices confirm that the differences are minimized under sunny and nearly aerosol-free sky
516 conditions. Comparing the performance on low-aerosol days to that on aerosol-laden, we conclude
517 that, particularly in the case of modelling 2-axis tracking systems, errors increase significantly. In
518 Tamanrasset, in particular, the errors are more than double.

519 3.5 Evaluation of the reliability of using the CAMS solar radiation time-series product in modelling
520 PV power potential

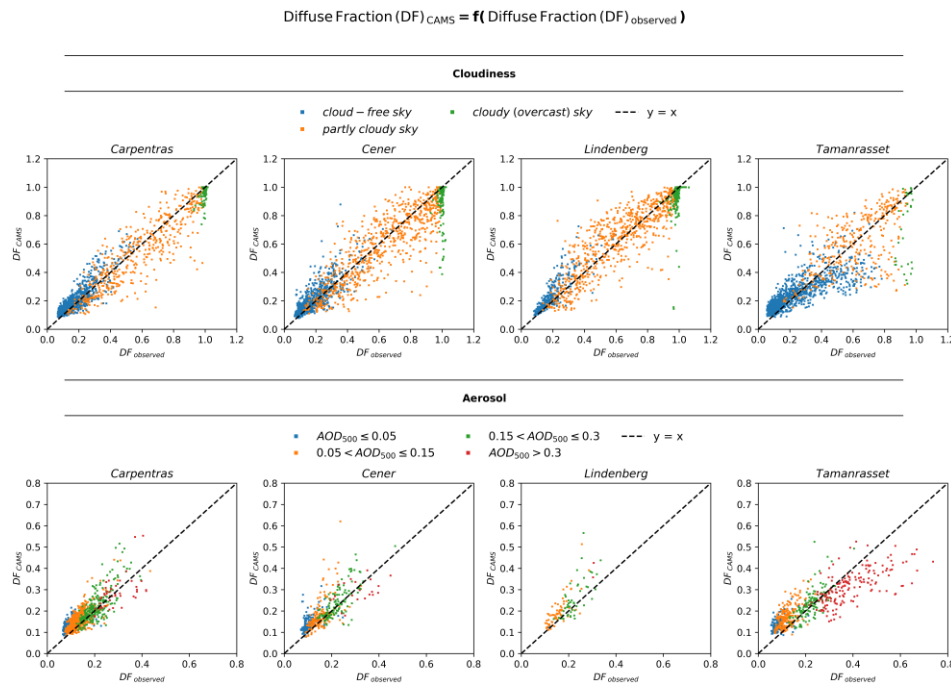
521 The aim of this section is to inspect the reliability of using the CAMS solar radiation time-series
522 product in modelling the PV power potential adapted to a certain location. A review of the existing
523 literature indicates a lack of studies directly examining the accuracy of using CAMS data for
524 assessing PV power potential. This is addressed by comparing the output power obtained from using
525 CAMS solar radiation data with that calculated using ground-based measurements. The analysis
526 focuses on the capability of CAMS to provide accurate estimates of both GHI as well as its individual
527 components.

528 In this section, we have excluded Izaña, because, due to its high altitude – as indicated through a
529 personal communication with Yves-Marie Saint-Drenan (2025) – comparable results would require

530 adjusting the measurements to the elevation of the stations, which is a complicated process and
531 beyond the scope of this study.

532 The CAMS-based diffuse fraction, compared to the observed, is presented in Figure 9 under different
533 prevailing conditions. We observe that the calculation of the diffuse component is subject to
534 significant uncertainty. Cloudiness is the primary uncertainty source, particularly under partly cloudy
535 conditions. Additionally, notable discrepancies related to aerosols emerge only in cases of very high
536 aerosol loading.

537



538
539 **Figure 9.** Comparison of the CAMS-based diffuse fraction estimated using BRL with the actual one
540 under diverse atmospheric conditions

541
542 In [Figure Fig. 10](#) we provide density scatter plots comparing the CAMS-based PV output power with
543 that computed from the ground-based BSRN data, aiming to illustrate how the uncertainty in the

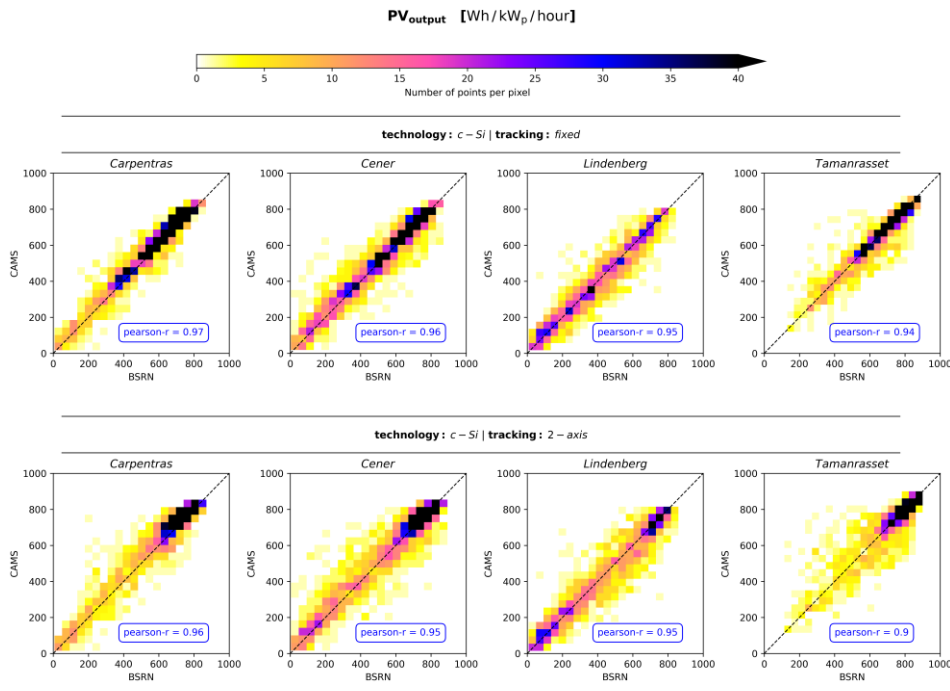
544 diffuse component estimates propagate to the calculation of power generation. Notably, there is a
545 much greater dispersion from the $y=x$ line in the case of simulating PV plants with 2-axis tracking
546 system, compared to that within the modelling of fixed panels. This outcome is attributed to the
547 increased sensitivity of the 2-axis tracking systems to the partitioning of global irradiance into its
548 components. Nevertheless, correlation coefficients are in all cases better than 0.9. **Additional**
549 **evaluation metrics are provided in the supplement (Tables S11-S14).**

Formatted: Font: Not Bold

550 **Additional evaluation metrics are provided in the supplement (Tables S9-S12).** Indicatively, we
551 **observe that under cloudless conditions, for fixed panels, RMSE ranges between 25.0 to 42.3**
552 **Wh/kWp/hour in Carpentras and 16.6 and 31.0 Wh/kWp/hour in Tamanrasset, with variations linked**
553 **to aerosol loading.** Similarly, MAE ranges from 20.0 to 36.9 Wh/kWp/hour in Carpentras and 11.9 to
554 **22.9 Wh/kWp/hour in Tamanrasset.** For 2-axis systems, RMSE and MAE follow similar trend, ranging
555 **from 28.8 to 49.9 Wh/kWp/hour and 22.3 to 44.1 Wh/kWp/hour, respectively, in Carpentras, and from**
556 **20.8 to 48.0 Wh/kWp/hour and 15.3 to 35.5 Wh/kWp/hour, respectively, in Tamanrasset.** Conversely,
557 **under cloudy conditions the errors are significantly increasing.** In Carpentras, as well as in Cener,
558 **and Lindenberg (according to the corresponding tables in the supplement) the errors peak under**
559 **partly cloudy conditions, with RMSE reaching up to 94.2 Wh/kWp/hour in Carpentras.** However, in
560 **Tamanrasset, the highest errors occur under overcast conditions, where RMSE and MAE for 2-axis**
561 **solar tracking systems reach 210.7 and 151.6 Wh/kWp/hour, respectively.** This exception can be
562 **interpreted through Figure 15, which illustrates that in the rare overcast scenes in Tamanrasset,**
563 **CAMS occasionally reports low diffuse fraction values instead of values close to 1, suggesting that**
564 **CAMS did not accurately represent cloudiness in these cases.**

565

566



567

Figure 10. Overview of the reliability of the CAMS-based PV power simulations

568

569 4. Conclusions

570 This study evaluated different solar radiation information that is commonly used for PV power
 571 modelling, and their implications for PV modelling accuracy. The optimal approach to include solar
 572 radiation information to PV power models such as GSEE is to use actual in-situ measurements of
 573 global and diffuse solar irradiance. Since measurements of the diffuse component are rarely
 574 available, it is common to use measurements of the GHI (if available) and retrieve the diffuse
 575 component using a model such as BRL. In the absence of in-situ measurements, other options
 576 include the use of datasets such as CAMS or even a radiative transfer model, provided that
 577 atmospheric inputs such as clearness index, aerosol optical depth (AOD), and other aerosol
 578 properties are available. This study evaluated these options and their implications for PV modelling
 579 accuracy.

580 The results highlighted the importance of having precise information for the distribution of solar
581 irradiance among its components in PV power modelling. The implementation of the BRL diffuse
582 fraction within GSEE serves as a practical, and under certain conditions, reliable solution to the
583 absence of detailed information for each component separately. Moreover, the integrated Climate
584 Data Interface submodule offers valuable prospects for investigating fluctuations in the solar PV
585 power generation across various timescales. In this context, the use of BRL has a key contribution
586 alongside the other computational procedures in processing climate datasets. [Previous studies on](#)
587 [PV power modelling approaches have not examined their reliability under diverse atmospheric](#)
588 [conditions, including the effects associated with cloudiness, aerosol loading, as well as aerosol](#)
589 [optical properties.](#)

590 The evaluation of the BRL's performance revealed a dependency of its reliability on the prevailing sky
591 conditions. [As a result, discrepancies arising from inconsistencies in diffuse fraction estimation](#)
592 [propagate to PV power generation. Within the modelling of PV plants equipped with 2-axis solar](#)
593 [tracking system, the deviations are much more pronounced relative to optimally inclined panels.](#) BRL
594 has excellent accuracy under totally clear sky scenes and still performs well for cloudless scenes
595 with moderate aerosol loading. In general, its accuracy is inversely proportional to the complexity of
596 the cloud scene. However, the model systematically underestimates the diffuse fraction under high-
597 loading conditions, such as during dust events. [Under such circumstances, this bias can potentially](#)
598 [lead to significant overestimation of power generation by up to 49.2 Wh/kWp/hour](#) [The discrepancies](#)
599 [arising from diffuse fraction estimation propagate to PV power generation and become particularly](#)
600 [pronounced in the modelling of 2-axis tracking systems. Indicatively, MAE under cloud-free scenes](#)
601 [with moderate aerosol loading, ranges between 2.2 to 6.6 Wh/kWp/hour for fixed panels and 4.7 to](#)
602 [15.0 Wh/kWp/hour for 2-axis tracking systems. Under partly cloudy conditions, where the cloud](#)
603 [scene is more complex, the MAE increases substantially, ranging from 12.4 to 25.8 Wh/kWp/hour for](#)
604 [fixed panels and from 23.5 to 55.1 Wh/kWp/hour for 2-axis tracking systems. Moreover, during](#)
605 [intense dust events, MAE can reach up to 49.2 Wh/kWp/hour in Tamanrasset, which is comparable](#)
606 [to that computed under partly cloudy conditions. Overall, the rMBE remains within the +5%, with the](#)
607 [exception of a limited cases under overcast conditions. The same analysis applied to CdTe panels](#)
608 [yielded similar results, with minor differences.](#)

609 Aiming to provide an indicative assessment of the financial impacts of the effect of desert dust
610 aerosols, we assume that the statistical indices calculated for Tamanrasset are representative of a

611 large-scale solar farm located in the Sahara region, with 500 MW installed PV capacity and systems
612 equipped with 2-axis solar tracking system. For this hypothetical solar farm, according to the value
613 of the Mean Absolute Error (MAE) on Table 4 for very high aerosol loading, we estimate that the
614 produced energy is $0.0492 \text{ [kWh/kWp/hour]} \times 500 \times 10^3 \text{ [kWp]} = 24600 \text{ [kWh/hour]}$
615 supposing 12 sunlight hours per day $\rightarrow \sim 295200 \text{ [kWh/day]}$ less than the expected from the PV power
616 simulations. According to the global average auction prices for selling produced energy back to the
617 grid in 2021 (IRENA, n.d.), the overestimations are equivalent to a financial loss of
618 $0.039 \text{ [USD/kWh]} \times 295200 \text{ [kWh/day]} \approx 11,500 \text{ USD/day}$. Therefore, site assessments that do
619 not correctly account for the impactdistribution of surface solar irradiance in the sky under desert
620 dust aerosotsaerosol conditions may overestimate financial performance and the annual financial
621 deficit could be accumulated to hundreds of thousands of US dollars per year.

622 Comparing the range of computed errors, we observe that the errors arising from employing CAMS
623 rather than using ground-based measurements, even when the diffuse fraction is not provided, are
624 higher across the overwhelming majority of the considered sky conditions. More specifically,
625 regarding the overall performance, MAE when using CAMS ranges between 33.7 and 46.1
626 Wh/kWp/hour, while with ground-based GHI measurements, MAE remains below 10 Wh/kWp/hour
627 within the modelling of systems with fixed panels and can reach up to 27.8 Wh/kWp/hour within the
628 modelling of 2-axis tracking systems. This outcome highlights the value of ground-based
629 measurements.

630 To sum up, achieving the highest quality PV power simulations necessitates high-quality, concurrent
631 measurements of solar irradiance components. In absence of this, the submodules included in the
632 GSEE package enable reliable simulations under the vast majority of prevailing sky conditions. CAMS
633 serves as a valuable data source for PV power modelling, but it cannot fully replace the precision and
634 reliability of using ground-based measurements. The integration of aerosol correction within the BRL
635 model opens new possibilities for further improvements in the modelling of solar energy systems. A
636 more comprehensive assessment would require measured PV output data; however, acquiring
637 simultaneous direct and diffuse irradiance measurements at the same location as the solar farms
638 remains challenging.

639

640 **Data availability**

641 The BSRN data are freely available on the BSRN web-page (<https://bsrn.awi.de/>). The AERONET
642 version 3 products are freely available from the AERONET website (<https://aeronet.gsfc.nasa.gov/>).
643 The CAMS radiation time-series are available from the Atmosphere Data Store
644 (<https://ads.atmosphere.copernicus.eu>). The rest of the data used in this paper are available upon
645 request from the authors.

646 **Author Contributions**

647 Conceptualization: NP and IF; Data curation: NP and KP; Formal analysis: NP; Funding acquisition:
648 CZ; Investigation: NP; Methodology: NP, IF, SK, AK and AG; Project administration: CZ; Resources: SP,
649 KP and LD; Software: NP; Supervision: IF; Validation: NP, IF and SP; Visualization: NP; Writing –
650 original draft: NP; Writing – review & editing: all authors

651 **Funding**

652 This work has been supported by the action titled “Support for upgrading the operation of the
653 National Network for Climate Change (CLIMPACT II)”, funded by the Public Investment Program of
654 Greece, General Secretary of Research and Technology/Ministry of Development and Investments.
655 Part of this work was also supported by the COST Action Harmonia (CA21119) supported by COST
656 (European Cooperation in Science and Technology). This work was partially funded by the
657 Copernicus Climate Change Service under contracts C3S2 _461-1_GR (Seasonal to decadal
658 predictions for national renewable energy management).

659 **Acknowledgments**

660 We thank the teams of the AERONET for ground measurements and maintenance, and CAMS for the
661 data production and distribution. We would like to thank the five site instrument operators and
662 technical staff of the BSRN network stations who made the ground-based measurements feasible.
663 A. Gkikas, J. Kapsomenakis, and C.S. Zerefos also acknowledge “CAMS2_82 Project: Evaluation and
664 Quality Control (EQC) of global products.”

665 **References**

666 Anderson, G., Clough, S., Kneizys, F., Chetwynd, J., & Shettle, E. (1986). *AFGL atmospheric*
667 *constituent profiles (0-120 km)* (Tech. Rep. AFGL-TR-86-0110). Air Force Geophysics Laboratory,
668 Hanscom Air Force Base.

669 Anderson, K. S., Hansen, C. W., Holmgren, W. F., Jensen, A. R., Mikofski, M. A., & Driesse, A.
670 (2023). *pvlib python: 2023 project update*. *Journal of Open Source Software*, 8(92), Article 5994.
671 <https://doi.org/10.21105/joss.05994>

672 Ångström, A. (1929). On the atmospheric transmission of sun radiation and on dust in the
673 air. *Geografiska Annaler*, 11(2), 156–166. <https://doi.org/10.1080/20014422.1929.11880498>

674 Barreto, Á., García, R. D., Guirado-Fuentes, C., Cuevas, E., Almansa, A. F., Milford, C., Toledano,
675 C., Expósito, F. J., Díaz, J. P., & León-Luis, S. F. (2022). Aerosol characterisation in the
676 subtropical eastern North Atlantic region using long-term AERONET
677 measurements. *Atmospheric Chemistry and Physics*, 22(17), 11105–11124.
678 <https://doi.org/10.5194/acp-22-11105-2022>

679 Blaga, R., Mares, O., Paulescu, E., Boata, R., Sabadus, A., Hategan, S.-M., Calinou, D., Stefu,
680 N., & Paulescu, M. (2024). Diffuse fraction as a tool for exploring the sensitivity of parametric
681 clear-sky models to changing aerosol conditions. *Solar Energy (Phoenix, Ariz.)*, 277(112731),
682 112731. <https://doi.org/10.1016/j.solener.2024.112731>

683 Blanc, P., Remund, J., & Vallance, L. (2017). Short-term solar power forecasting based on
684 satellite images. In *Renewable Energy Forecasting* (pp. 179–198). Elsevier.

685 Boland, J. W., Scott, L., & Luther, M. (2001). *Modelling the diffuse fraction of global solar
686 radiation on a horizontal surface*. *Environmetrics*, 12(2), 103–116. [https://doi.org/10.1002/1099-095X\(200103\)12:2<103::AID-ENV447>3.0.CO;2-2](https://doi.org/10.1002/1099-
687 095X(200103)12:2<103::AID-ENV447>3.0.CO;2-2)

688 Buras, R., Dowling, T., & Emde, C. (2011). New secondary-scattering correction in DISORT with
689 increased efficiency for forward scattering. *Journal of Quantitative Spectroscopy & Radiative
690 Transfer*, 112(12), 2028–2034. <https://doi.org/10.1016/j.jqsrt.2011.03.019>

691 Cañadillas-Ramallo, D., Moutaoikil, A., Shephard, L. E., & Guerrero-Lemus, R. (2022). The
692 influence of extreme dust events in the current and future 100% renewable power scenarios in
693 Tenerife. *Renewable Energy*, 184, 948–959. <https://doi.org/10.1016/j.renene.2021.12.013>

694 Copernicus Atmosphere Monitoring Service. (2020). *CAMS solar radiation time-series*.
695 Copernicus Atmosphere Monitoring Service (CAMS) Atmosphere Data Store.
696 <https://doi.org/10.24381/5cab0912>

697 Cuevas, E., Romero-Campos, P. M., Kouremeti, N., Kazadzis, S., Räisänen, P., García, R. D.,
698 Barreto, A., Guirado-Fuentes, C., Ramos, R., Toledano, C., Almansa, F., & Gröbner, J. (2019).
699 Aerosol optical depth comparison between GAW-PFR and AERONET-Cimel radiometers from
700 long-term (2005–2015) 1 min synchronous measurements. *Atmospheric Measurement
Techniques*, 12(8), 4309–4337. <https://doi.org/10.5194/amt-12-4309-2019>

701 Driemel, A., Augustine, J., Behrens, K., Colle, S., Cox, C., Cuevas-Agulló, E., Denn, F. M., Duprat,
702 T., Fukuda, M., Grobe, H., Haeffelin, M., Hodges, G., Hyett, N., Ijima, O., Kallis, A., Knap, W.,
703 Kustov, V., Long, C. N., Longenecker, D., ... König-Langlo, G. (2018). Baseline Surface Radiation
704 Network (BSRN): structure and data description (1992–2017). *Earth System Science
Data*, 10(3), 1491–1501. <https://doi.org/10.5194/essd-10-1491-2018>

705 Dubey, S., Sarvaiya, J. N., & Seshadri, B. (2013). Temperature dependent photovoltaic (PV)
706 efficiency and its effect on PV production in the world – A review. *Energy Procedia*, 33, 311–321.
707 <https://doi.org/10.1016/j.egypro.2013.05.072>

708 Dubovik, O., Holben, B., Eck, T. F., Smirnov, A., Kaufman, Y. J., King, M. D., Tanré, D., & Slutsker, I.
709 (2002). Variability of absorption and optical properties of key aerosol types observed in
710 worldwide locations. *Journal of the Atmospheric Sciences*, 59(3), 590–608.
711 [https://doi.org/10.1175/1520-0469\(2002\)059<0590:voaaop>2.0.co;2](https://doi.org/10.1175/1520-0469(2002)059<0590:voaaop>2.0.co;2)

712 Dubovik, O., & King, M. D. (2000). A flexible inversion algorithm for retrieval of aerosol optical
713 properties from Sun and sky radiance measurements. *Journal of Geophysical
Research*, 105(D16), 20673–20696. <https://doi.org/10.1029/2000jd900282>

714 Edenhofer, O., Pichs-Madruga, R., Sokona, Y., Seyboth, K., Kadner, S., Zwickel, T., Eickemeier, P.,
715 Hansen, G., Schlömer, S., & Von Stechow, C. (Eds.). (2011). *Renewable energy sources and
716 climate change mitigation: Special report of the intergovernmental panel on climate change*.
717 Cambridge University Press.

718 Emde, C., Buras-Schnell, R., Kylling, A., Mayer, B., Gasteiger, J., Hamann, U., Kylling, J., Richter,
719 B., Pause, C., Dowling, T., & Bugliaro, L. (2016). The libRadtran software package for radiative
720 transfer calculations (version 2.0.1). *Geoscientific Model Development*, 9(5), 1647–1672.
721 <https://doi.org/10.5194/gmd-9-1647-2016>

725 Faid, A., Smara, Y., Caselles, V., & Khireddine, A. (2012). Evaluation of the Saharan aerosol
726 impact on solar radiation over the Tamanrasset area, Algeria. *International Journal of Advanced*
727 *Research in Engineering and Technology*, 3(1), 24–32.

728 Fountoulakis, I., Kosmopoulos, P., Papachristopoulou, K., Raptis, I.-P., Mamouri, R.-E., Nisantzi,
729 A., Gkikas, A., Witthuhn, J., Bley, S., Moustaka, A., Buehl, J., Seifert, P., Hadjimitsis, D. G.,
730 Kontoes, C., & Kazadzis, S. (2021). Effects of aerosols and clouds on the levels of surface solar
731 radiation and solar energy in Cyprus. *Remote Sensing*, 13(12), 2319.
732 <https://doi.org/10.3390/rs13122319>

733 Fountoulakis, I., Papachristopoulou, K., Proestakis, E., Amiridis, V., Kontoes, C., & Kazadzis, S.
734 (2022). Effect of aerosol vertical distribution on the modeling of solar radiation. *Remote*
735 *Sensing*, 14(5), 1143. <https://doi.org/10.3390/rs14051143>

736 Giles, D. M., Sinyuk, A., Sorokin, M. G., Schafer, J. S., Smirnov, A., Slutsker, I., Eck, T. F., Holben,
737 B. N., Lewis, J. R., Campbell, J. R., Welton, E. J., Korkin, S. V., & Lyapustin, A. I. (2019).
738 Advancements in the Aerosol Robotic Network (AERONET) Version 3 database – automated
739 near-real-time quality control algorithm with improved cloud screening for Sun photometer
740 aerosol optical depth (AOD) measurements. *Atmospheric Measurement Techniques*, 12(1),
741 169–209. <https://doi.org/10.5194/amt-12-169-2019>

742 Holben, B. N., Eck, T. F., Slutsker, I., Tanré, D., Buis, J. P., Setzer, A., Vermote, E., Reagan, J. A.,
743 Kaufman, Y. J., Nakajima, T., Lavenu, F., Jankowiak, I., & Smirnov, A. (1998). AERONET—A
744 federated instrument network and data archive for aerosol characterization. *Remote Sensing of*
745 *Environment*, 66(1), 1–16. [https://doi.org/10.1016/s0034-4257\(98\)00031-5](https://doi.org/10.1016/s0034-4257(98)00031-5)

746 Hou, X., Wild, M., Folini, D., Kazadzis, S., & Wohland, J. (2021). Climate change impacts on solar
747 power generation and its spatial variability in Europe based on CMIP6. *Earth System*
748 *Dynamics*, 12(4), 1099–1113. <https://doi.org/10.5194/esd-12-1099-2021>

749 Huld, T., Gottschalg, R., Beyer, H. G., & Topič, M. (2010). Mapping the performance of PV
750 modules, effects of module type and data averaging. *Solar Energy (Phoenix, Ariz.)*, 84(2), 324–
751 338. <https://doi.org/10.1016/j.solener.2009.12.002>

752 Intergovernmental Panel on Climate Change (IPCC). (2023). *Climate change 2022 – impacts,
753 adaptation and vulnerability: Working group II contribution to the sixth assessment report of the*

754 *intergovernmental panel on climate change*. Cambridge University Press.

755 <https://doi.org/10.1017/9781009325844>

756 Jacovides, C. P., Tymvios, F. S., Assimakopoulos, V. D., & Kaltsounides, N. A. (2006).

757 Comparative study of various correlations in estimating hourly diffuse fraction of global solar

758 radiation. *Renewable Energy*, 31(15), 2492–2504. <https://doi.org/10.1016/j.renene.2005.11.009>

759 Kakran, S., Rathore, J. S., Sidhu, A., & Kumar, A. (2024). Solar energy advances and CO₂

760 emissions: A comparative review of leading nations' path to sustainable future. *Journal of*

761 *Cleaner Production*, 475(143598), 143598. <https://doi.org/10.1016/j.jclepro.2024.143598>

762 Kato, S., Ackerman, T. P., Mather, J. H., & Clothiaux, E. E. (1999). The k-distribution method and

763 correlated-k approximation for a shortwave radiative transfer model. *Journal of Quantitative*

764 *Spectroscopy & Radiative Transfer*, 62(1), 109–121. [https://doi.org/10.1016/s0022-4073\(98\)00075-2](https://doi.org/10.1016/s0022-4073(98)00075-2)

765

766 Kazantzidis, A., Tzoumanikas, P., Blanc, P., Massip, P., Wilbert, S., & Ramirez-Santigosa, L.

767 (2017). Short-term forecasting based on all-sky cameras. In *Renewable Energy Forecasting* (pp.

768 153–178). Elsevier.

769

770 [Kosmopoulos, P., Kazadzis, S., El-Askary, H., Taylor, M., Gkikas, A., Proestakis, E., Kontoes, C., & El-Khayat, M. \(2018\). Earth-Observation-based estimation and forecasting of particulate matter impact on solar energy in Egypt. *Remote Sensing*, 10\(12\), 1870.](#)

771

772 <https://doi.org/10.3390/rs10121870>

773

774 [Kouklaki, D., Kazadzis, S., Raptis, I.-P., Papachristopoulou, K., Fountoulakis, I., & Eleftheratos, K. \(2023\). Photovoltaic spectral responsivity and efficiency under different aerosol conditions. *Energies*, 16\(18\), 6644.](#) <https://doi.org/10.3390/en16186644>

775

776

777

778 Lauret, P., Boland, J., & Ridley, B. (2013). Bayesian statistical analysis applied to solar radiation

779 modelling. *Renewable Energy*, 49, 124–127. <https://doi.org/10.1016/j.renene.2012.01.049>

780 Liu, B. Y. H., & Jordan, R. C. (1960). The interrelationship and characteristic distribution of
781 direct, diffuse and total solar radiation. *Solar Energy (Phoenix, Ariz.)*, 4(3), 1–19.
782 [https://doi.org/10.1016/0038-092x\(60\)90062-1](https://doi.org/10.1016/0038-092x(60)90062-1)

783 Logothetis, S.-A., Salamalikis, V., & Kazantzidis, A. (2020). Aerosol classification in Europe,
784 Middle East, North Africa and Arabian Peninsula based on AERONET Version 3. *Atmospheric*
785 *Research*, 239(104893), 104893. <https://doi.org/10.1016/j.atmosres.2020.104893>

786 Long, C., & Dutton, E. (2010). *BSRN Global Network recommended QC tests, V2.x*.
787 https://epic.awi.de/id/eprint/30083/1/BSRN_recommended_QC_tests_V2.pdf

788 Mayer, B., & Kylling, A. (2005). Technical note: The libRadtran software package for radiative
789 transfer calculations - description and examples of use. *Atmospheric Chemistry and*
790 *Physics*, 5(7), 1855–1877. <https://doi.org/10.5194/acp-5-1855-2005>

791 McMahan, A. C., Grover, C. N., & Vignola, F. E. (2013). Evaluation of resource risk in solar-
792 project financing. In *Solar Energy Forecasting and Resource Assessment* (pp. 81–95). Elsevier.

793 Owusu, P. A., & Asumadu-Sarkodie, S. (2016). A review of renewable energy sources,
794 sustainability issues and climate change mitigation. *Cogent Engineering*, 3(1), 1167990.
795 <https://doi.org/10.1080/23311916.2016.1167990>

796 Papachristopoulou, K., Fountoulakis, I., Bais, A. F., Psiloglou, B. E., Papadimitriou, N., Raptis, I.-
797 P., Kazantzidis, A., Kontoes, C., Hatzaki, M., & Kazadzis, S. (2024). Effects of clouds and
798 aerosols on downwelling surface solar irradiance nowcasting and short-term
799 forecasting. *Atmospheric Measurement Techniques*, 17(7), 1851–1877.
800 <https://doi.org/10.5194/amt-17-1851-2024>

801 Papachristopoulou, K., Fountoulakis, I., Gkikas, A., Kosmopoulos, P. G., Nastos, P. T., Hatzaki,
802 M., & Kazadzis, S. (2022). 15-year analysis of direct effects of total and dust aerosols in solar
803 radiation/energy over the Mediterranean Basin. *Remote Sensing*, 14(7), 1535.
804 <https://doi.org/10.3390/rs14071535>

805 Paulescu, E., & Blaga, R. (2019). A simple and reliable empirical model with two predictors for
806 estimating 1-minute diffuse fraction. *Solar Energy (Phoenix, Ariz.)*, 180, 75–84.
807 <https://doi.org/10.1016/j.solener.2019.01.029>

808 Pedro, H. T. C., Inman, R. H., & Coimbra, C. F. M. (2017). Mathematical methods for optimized
809 solar forecasting. In *Renewable Energy Forecasting* (pp. 111–152). Elsevier.

810 Pfenninger, S., & Staffell, I. (2016). Long-term patterns of European PV output using 30 years of
811 validated hourly reanalysis and satellite data. *Energy (Oxford, England)*, 114, 1251–1265.
812 <https://doi.org/10.1016/j.energy.2016.08.060>

813 [Raptis, I.-P., Kazadzis, S., Fountoulakis, I., Papachristopoulou, K., Kouklaki, D., Psiloglou, B. E.,](#)
814 [Kazantzidis, A., Benetatos, C., Papadimitriou, N., & Eleftheratos, K. \(2023\). Evaluation of the](#)
815 [solar energy nowcasting system \(SENSE\) during a 12-months intensive measurement campaign](#)
816 [in Athens, Greece. *Energies*, 16\(14\), 5361. https://doi.org/10.3390/en16145361](#)

817

818 Qu, Z., Oumbe, A., Blanc, P., Espinar, B., Gesell, G., Gschwind, B., Klüser, L., Lefèvre, M.,
819 Saboret, L., Schroedter-Homscheidt, M., & Wald, L. (2017). Fast radiative transfer
820 parameterisation for assessing the surface solar irradiance: The Heliosat-4
821 method. *Meteorologische Zeitschrift*, 26(1), 33–57. <https://doi.org/10.1127/metz/2016/0781>

822 Renewables Ninja. (n.d.). *Climate data interface*. GSEE Documentation.
823 <https://gsee.readthedocs.io/en/latest/climatedata-interface/>

824 Ridley, B., Boland, J., & Lauret, P. (2010). Modelling of diffuse solar fraction with multiple
825 predictors. *Renewable Energy*, 35(2), 478–483. <https://doi.org/10.1016/j.renene.2009.07.018>

826 Schroedter-Homscheidt, M., Azam, F., Betcke, J., Hanrieder, N., Lefèvre, M., Saboret, L., &
827 Saint-Drenan, Y. -M. (2022). Surface solar irradiation retrieval from MSG/SEVIRI based on
828 APOLLO Next Generation and HELIOSAT-4 methods. *Meteorologische Zeitschrift*, 31(6), 455–
829 476. <https://doi.org/10.1127/metz/2022/1132>

830 Shettle, E. (1989). Models of aerosols, clouds, and precipitation for atmospheric propagation
831 studies. In *Atmospheric propagation in the UV, visible, IR and mm-region and related system*
832 *aspects* (AGARD Conference Proceedings No. 454). NATO Advisory Group for Aerospace
833 Research and Development.

834 Stoffel, T. (2013). Terms and Definitions. In *Solar Energy Forecasting and Resource*
835 *Assessment* (pp. 1–19). Elsevier.

836 Toledano, C., González, R., Fuertes, D., Cuevas, E., Eck, T. F., Kazadzis, S., Kouremeti, N.,
837 Gröbner, J., Goloub, P., Blarel, L., Román, R., Barreto, Á., Berjón, A., Holben, B. N., & Cachorro,
838 V. E. (2018). Assessment of Sun photometer Langley calibration at the high-elevation sites
839 Mauna Loa and Izaña. *Atmospheric Chemistry and Physics*, 18(19), 14555–14567.
840 <https://doi.org/10.5194/acp-18-14555-2018>

841 WMO. (2021). *Guide to instruments and methods of observation* (WMO-No. 8).
842 https://library.wmo.int/doc_num.php?explnum_id=57838

843 Yang, D. (2019). SolarData package update v1.1: R functions for easy access of Baseline
844 Surface Radiation Network (BSRN). *Solar Energy (Phoenix, Ariz.)*, 188, 970–975.
845 <https://doi.org/10.1016/j.solener.2019.05.068>

846

847

848

849

Supplement

2 Nomenclature

Acronym	Definition
AEMET	Agencia Estatal de Meteorología: Meteorological State Agency of Spain
AERONET	AErosol RObotic NETwork
AE	Angström Exponent
AOD	Aerosol Optical Depth
BRL	Boland-Ridley-Lauret diffuse fraction model
BSRN	Baseline Surface Radiation Network
CAMS	Copernicus Atmosphere Monitoring Service: ECMWF tool for atmospheric composition knowledge
GENER	Centro Nacional de Energías Renovables, National Renewable Energy Centre of Spain
DHI	Diffuse Horizontal Irradiance
DNI	Direct Normal Irradiance
DWD	Deutscher Wetterdienst: German Meteorological Service
ECMWF	European Centre for Medium-Range Weather Forecasts
FMF	Fine Mode Fraction
gg	Assymetry factor
GHI	Global Horizontal Irradiance
GSEE	Global Solar Energy Estimator
IARC	Izaña Atmospheric Research Center: AEMET Observatory of Izaña, Tenerife, Spain
MAE	Man Absolute Error
MBE	Mean Bias Error
Md	Median
MOL-RAO	Meteorologisches Observatorium Lindenberg, Richard-Aßmann-Observatorium: DWD Observatory Lindenberg, Lindenberg (Tauche), Germany
NEO	Navarino Environmental Observatory, Messinia, Greece

OMN	Office national de la météorologie, "Météo Algérie": National Meteorological Office of Algeria
PDFs	Probability Density Functions
PMOD/WRC	Physikalisch-Meteorologisches Observatorium Davos / World Radiation Center, Davos, Switzerland
PV	Photovoltaic
QC	Quality Check
r	Weighted correlation coefficient
rMBE	Relative Mean Bias Error
RMSE	Root Mean Square Error
RTM	Radiative Transfer Model
SDA	Spectral Deconvolution Algorithm
SSA	Single Scattering Albedo
SV	Solar Visibility
SZA	Solar Zenith Angle
TOC	Total Ozone Column (in DU)
TPM	Faculty of Technology, Policy, and Management, Delft, the Netherlands
UTC	Coordinated Universal Time
WMO	World Meteorological Organisation

3

4

5 **Evaluation Metrics**

6 The formulas for the evaluation metrics used are the following:

7 1. Root Mean Square Error (RMSE)

8
$$RMSE = \sqrt{\frac{1}{N} \sum (x_{mod} - x_{obs})^2}$$

9 2. Mean Absolute Error (MAE)

10
$$MAE = \frac{1}{N} \sum |x_{mod} - x_{obs}|$$

11 3. relative Mean Bias Error (rMBE)

12

$$rMBE = \frac{1}{N} \sum \left(\frac{x_{mod} - x_{obs}}{x_{obs}} \right) \times 100\%$$

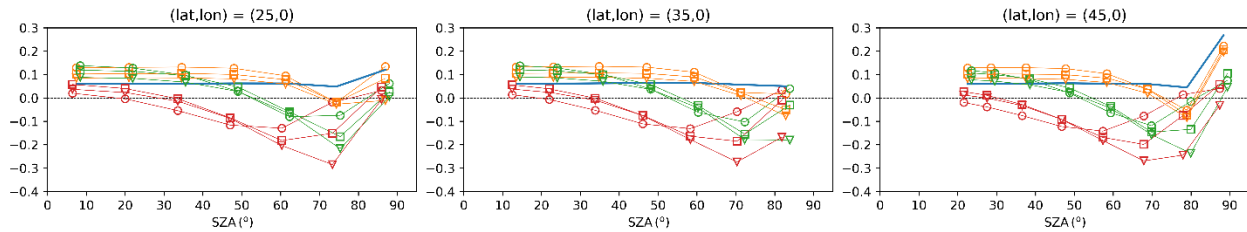
13

...

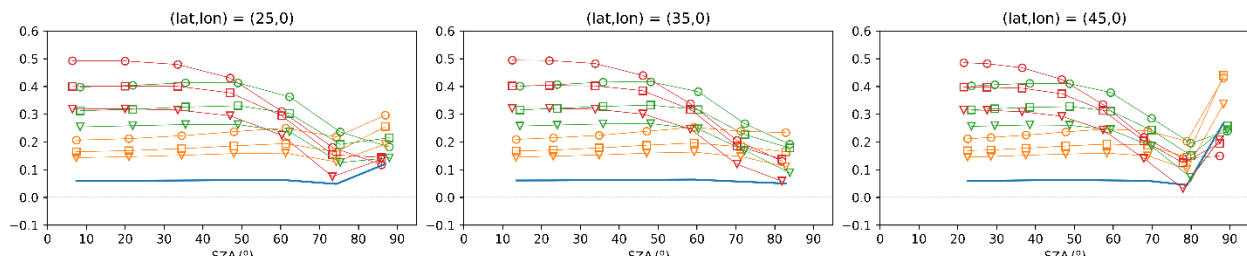
Diffuse Fraction (DF) _{libRadtran} – Diffuse Fraction (DF) _{BRL} = $f(sza)$

clearsky $AOD_{500} = 0.6$ \circ Δ \square
 $AOD_{500} = 0.2$ $AOD_{500} = 1.0$ \square \square \square

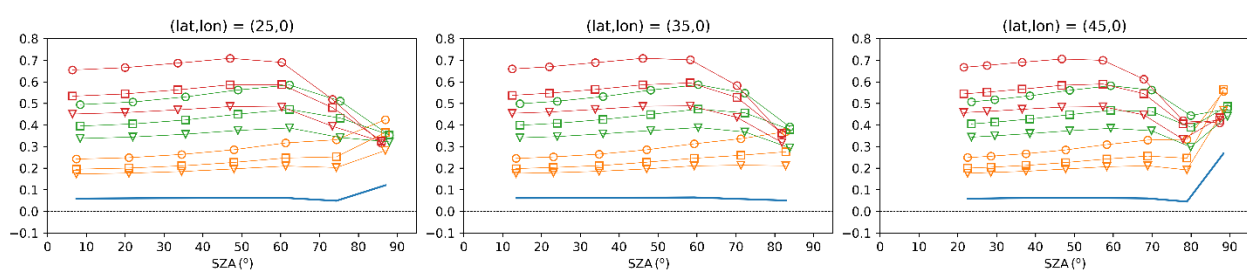
ssa : 0.7 | altitude : 100 m



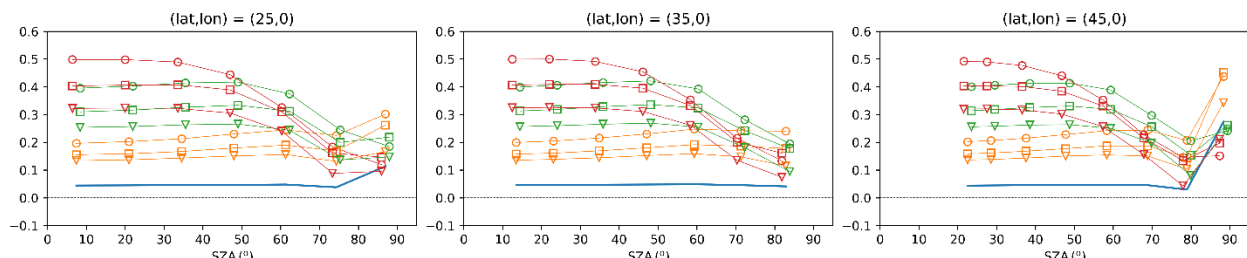
ssa : 0.9 | altitude : 100 m



ssa : 1.0 | altitude : 100 m



ssa : 0.9 | altitude : 2 km

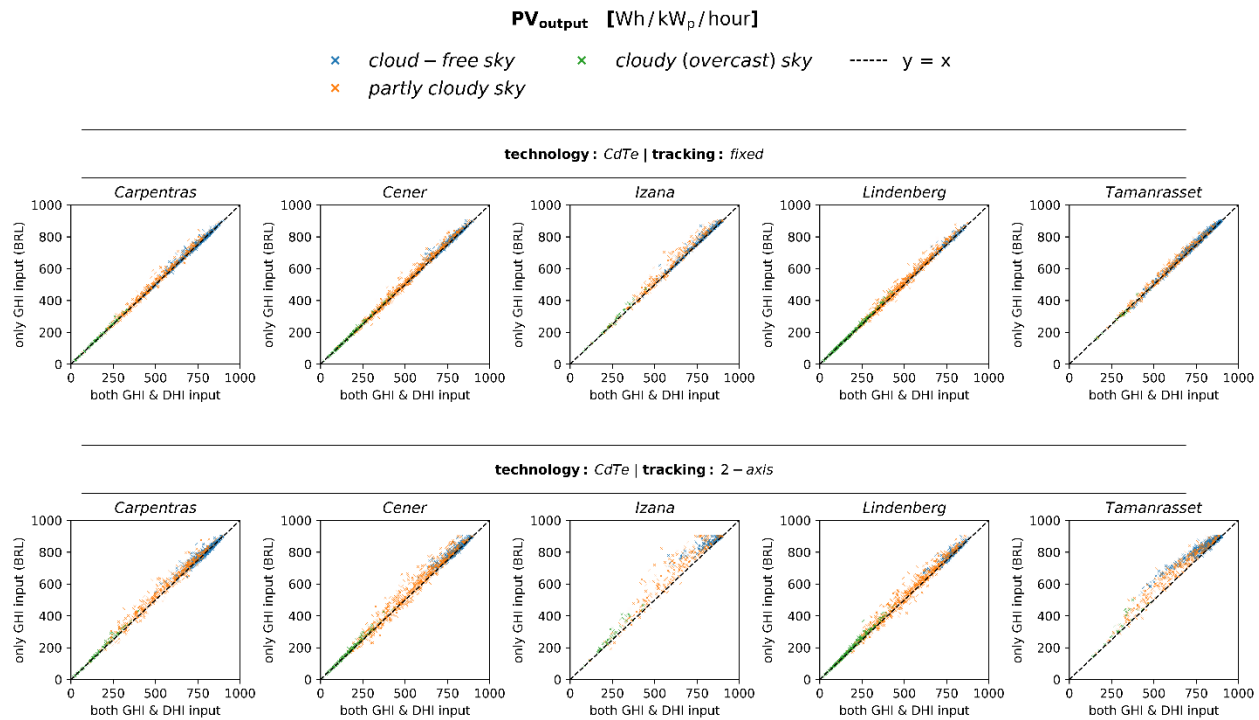


14

15 **Figure S1.** Difference between the diffuse fraction derived directly from the computations of DHI
 16 and GHI using libRadtran and the one estimated by applying BRL to the libRadtran-computed GHI
 17 for surface albedo 0.8

18 ...

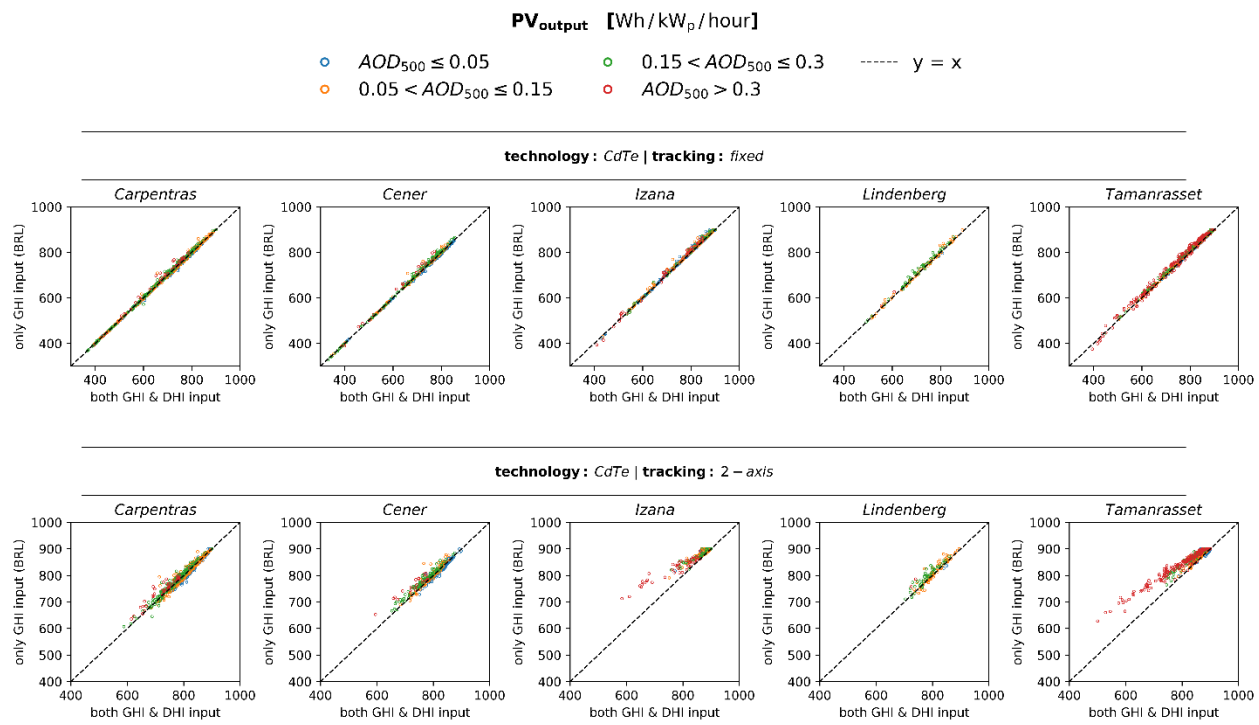
19



20

21 **Figure S2.** Comparison of the estimated hourly PV power generation between simulations
 22 performed using GSEE with input data consisting of either only GHI or both GHI and DHI under
 23 varying cloudiness conditions for panels with CdTe technology

24



25

26 **Figure S3.** Comparison of the estimated hourly PV power generation between simulations
 27 performed using GSEE with input data consisting of either only GHI or both GHI and DHI under
 28 varying aerosol conditions for panels with CdTe technology

29

...

30 **Table S1.** Evaluation metrics for GSEE performance within hourly intervals in Carpentras,
 31 comparing simulations with diffuse fraction from measurements and from the BRL model

STATION: Carpentras		fixed panels			2-axis tracking		
		RMSE (Wh/kW _p /hour)	MAE (Wh/kW _p /hour)	rMBE (%)	RMSE (Wh/kW _p /hour)	MAE (Wh/kW _p /hour)	rMBE (%)
All-Sky scenes		12.6	6.6	0.8	20.8	12.5	1.2
All-Sky scenes (cloudiness)	cloud-free	9.2	4.6	0.4	14.8	8.7	0.5
	partly cloudy	19.5	12.5	2.3	32.5	23.9	3.8
	cloudy (overcast)	5.8	3.0	2.0	10.5	6.1	4.6
Cloudless- Sky scenes (aerosol load)	tow	4.7	3.4	-0.4	9.5	7.5	-0.8
	moderate	4.3	2.2	0.1	7.8	4.7	0.0
	high	6.4	4.0	0.6	11.0	7.8	0.9
	very high	14.9	10.2	1.6	22.7	17.2	2.6

32

33 **Table S2.** Evaluation metrics for GSEE performance within hourly intervals in Tamanrasset,
 34 comparing simulations with diffuse fraction from measurements and from the BRL model.

STATION: Tamanrasset		fixed panels			2-axis tracking		
		RMSE (Wh/kWp/hour)	MAE (Wh/kWp/hour)	rMBE (%)	RMSE (Wh/kWp/hour)	MAE (Wh/kWp/hour)	rMBE (%)
All-Sky scenes		13.6	9.3	1.0	40.4	27.8	9.8
All-Sky scenes (cloudiness)	cloud-free	11.5	8.0	0.8	35.3	23.4	2.9
	partly cloudy	20.1	15.0	2.0	56.1	45.7	8.1
	cloudy (overcast)	8.4	5.2	-0.1	45.3	30.1	11.2
Cloudless-Sky scenes (aerosol load)	low	3.2	2.0	0.2	6.6	4.0	0.3
	moderate	5.4	4.6	0.6	13.0	10.5	1.2

35

36 **Table S3S1.** Evaluation metrics for GSEE performance within hourly intervals in Cener, comparing
 37 simulations with diffuse fraction from measurements and from the BRL model.

STATION: Cener		fixed panels			2-axis tracking		
		RMSE (Wh/kWp/hour)	MAE (Wh/kWp/hour)	rMBE (%)	RMSE (Wh/kWp/hour)	MAE (Wh/kWp/hour)	rMBE (%)
All-Sky scenes		14.5	8.2	1.2	27.1	16.7	2.3
All-Sky scenes (cloudiness)	cloud-free	11.7	6.4	0.8	19.5	11.9	1.3
	partly cloudy	19.3	12.4	2.0	37.5	26.4	4.1
	cloudy (overcast)	4.7	2.7	1.6	11.2	6.3	4.6
Cloudless-Sky scenes (aerosol load)	clear sky / low	4.0	2.5	-0.2	7.9	5.5	-0.4
	moderate	6.9	3.1	0.4	11.4	6.2	0.6
	high	8.7	6.2	1.0	15.4	12.8	1.8
	very high	NaN	NaN	NaN	NaN	NaN	NaN

38

39 **Table S4S2.** Evaluation metrics for GSEE performance within hourly intervals in Lindenberg,
 40 comparing simulations with diffuse fraction from measurements and from the BRL model.

STATION: Lindenberg		fixed panels			2-axis tracking		
		RMSE (Wh/kWp/hour)	MAE (Wh/kWp/hour)	rMBE (%)	RMSE (Wh/kWp/hour)	MAE (Wh/kWp/hour)	rMBE (%)
All-Sky scenes		16.0	9.7	1.8	26.1	17.0	2.7
All-Sky scenes (cloudiness)	cloud-free	11.8	6.7	0.9	20.7	13.5	1.4
	partly cloudy	20.4	13.9	2.3	32.4	23.5	3.5
	cloudy (overcast)	6.7	3.6	2.4	11.7	6.5	4.6

Cloudless-Sky scenes	clear sky / low	NaN	NaN	NaN	NaN	NaN	NaN
	moderate	8.9	5.5	0.5	14.9	9.7	0.6
	high	12.6	10.3	1.4	19.5	15.9	2.0
	very high	NaN	NaN	NaN	NaN	NaN	NaN

41

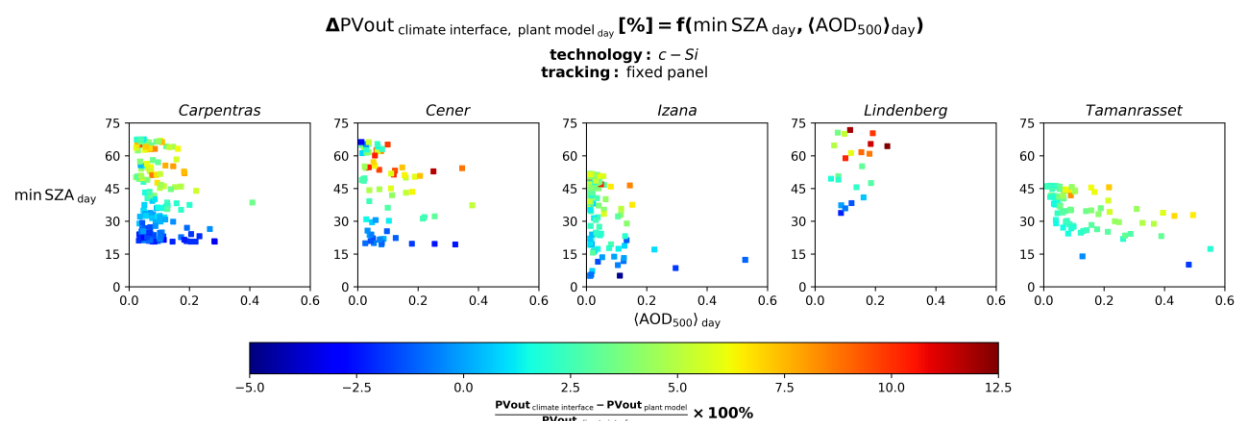
42 **Table S5S3.** Evaluation metrics for GSEE performance within hourly intervals in Izana, comparing
43 simulations with diffuse fraction from measurements and from the BRL model.

STATION: Izana		fixed panels			2-axis tracking		
		RMSE (Wh/kWp/hour)	MAE (Wh/kWp/hour)	rMBE (%)	RMSE (Wh/kWp/hour)	MAE (Wh/kWp/hour)	rMBE (%)
All-Sky scenes		20.0	11.3	1.5	41.5	22.3	2.8
All-Sky scenes (cloudiness)	cloud-free	12.3	7.2	0.9	26.6	12.7	1.5
	partly cloudy	36.1	25.8	4.3	73.4	55.1	9.3
	cloudy (overcast)	16.8	11.8	4.6	35.5	26.0	11.8
Cloudless-Sky scenes (aerosol load)	clear sky / low	6.8	4.8	0.6	7.8	3.7	0.4
	moderate	9.3	6.5	0.9	20.8	15.0	1.8
	high	11.2	8.6	1.1	31.4	26.2	3.3
	very high	14.1	11.8	1.4	64.5	52.1	7.3

44

45

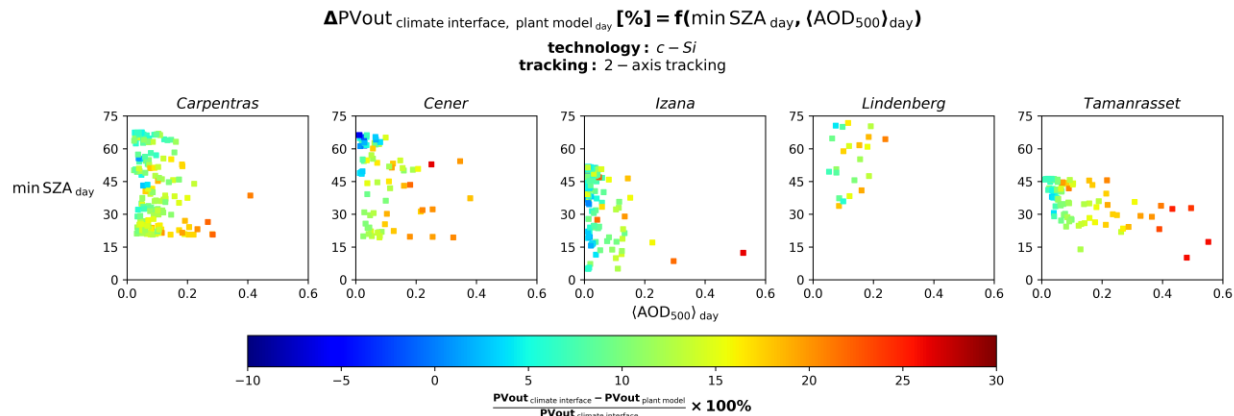
46



47

48 **Figure S4.** Percentage differences between the daily PV output estimated using the climate
49 interface and the corresponding daily sums from hourly simulations as function of minimum daily
50 SZA and mean daily aerosol load for fixed panels

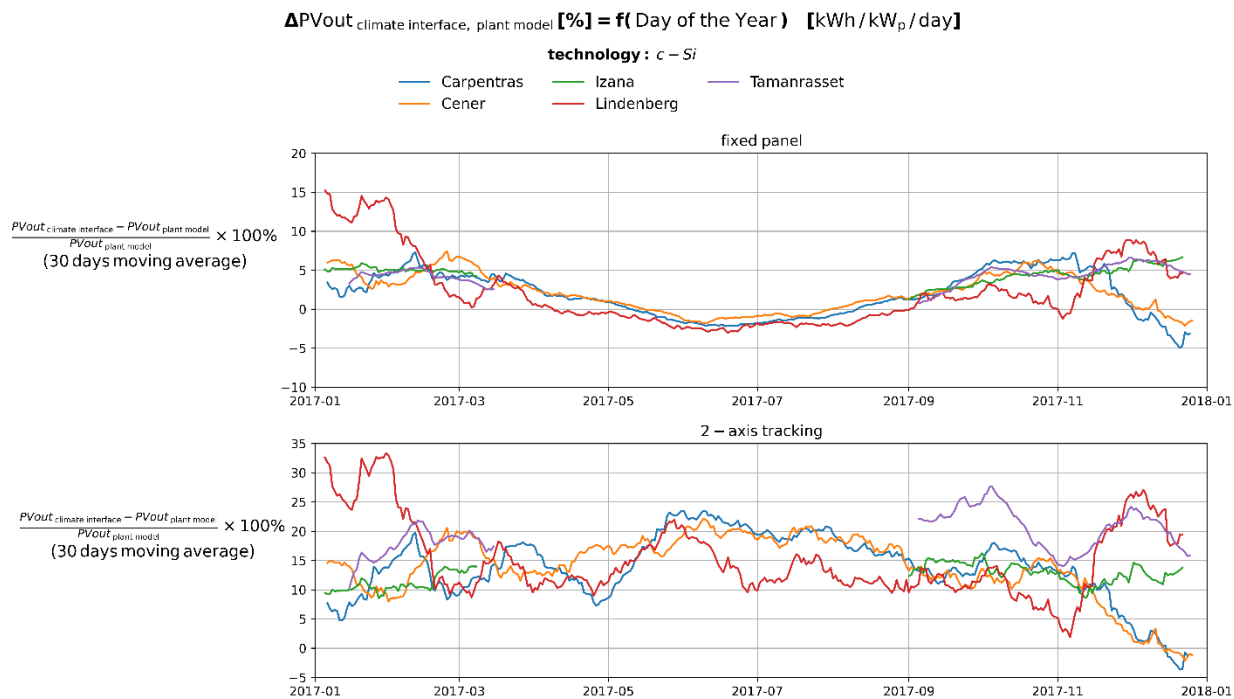
51



52

53 **Figure S5.** Percentage differences between the daily PV output estimated using the climate
 54 interface and the corresponding daily sums from hourly simulations as function of minimum daily
 55 SZA and mean daily aerosol load for panels with 2-axis tracking

56



57

58 **Figure S6.** Time-series of the percentage differences between the daily PV output estimated using
 59 the climate interface and the corresponding daily sums from hourly simulations

60

61

...

62 **Table S6S4.** Evaluation metrics assessing the reliability of GSEE Climate Data Interface in
 63 estimating total daily PV output power in Carpentras

STATION: Carpentras		fixed panels			2-axis tracking		
		RMSE (kWh/kWp/day)	MAE (kWh/kWp/day)	rMBE (%)	RMSE (kWh/kWp/day)	MAE (kWh/kWp/day)	rMBE (%)
All Days		0.22	0.17	1.7	1.24	1.08	15.5
Sunny (cloudless) Days		0.19	0.15	1.8	1.19	1.08	14.1
Sunny Days: average aerosol load	very-low aerosol	0.18	0.15	2.1	0.82	0.72	10.0
	aerosol-laden	0.19	0.16	1.7	1.28	1.20	15.3

64

65 **Table S7S5.** Evaluation metrics assessing the reliability of GSEE Climate Data Interface in
 66 estimating total daily PV output power in Tamanrasset

STATION: Tamanrasset		fixed panels			2-axis tracking		
		RMSE (kWh/kWp/day)	MAE (kWh/kWp/day)	rMBE (%)	RMSE (kWh/kWp/day)	MAE (kWh/kWp/day)	rMBE (%)
All Days		0.24	0.22	3.4	1.45	1.34	19.0
Sunny (cloudless) Days		0.22	0.20	3.4	1.20	1.11	14.4
Sunny Days: average aerosol load	very-low aerosol	0.15	0.14	2.5	0.66	0.62	7.7
	aerosol-laden	0.24	0.22	3.7	1.37	1.31	17.3

67

68 **Table S8S6.** Evaluation metrics assessing the reliability of GSEE Climate Data Interface in
 69 estimating total daily PV output power in Cener

STATION: Cener		fixed panels			2-axis tracking		
		RMSE (kWh/kWp/day)	MAE (kWh/kWp/day)	rMBE (%)	RMSE (kWh/kWp/day)	MAE (kWh/kWp/day)	rMBE (%)
All Days		0.24	0.18	2.5	1.28	1.08	16.8
Sunny (cloudless) Days		0.26	0.21	3.3	1.15	1.00	13.6
Sunny Days (average aerosol load)	aerosol-free	0.18	0.15	2.4	0.73	0.60	7.6
	aerosol-laden	0.30	0.24	4.0	1.37	1.28	17.8

70

71 **Table S9S7.** Evaluation metrics assessing the reliability of GSEE Climate Data Interface in
 72 estimating total daily PV output power in Lindenberg

STATION: Lindenberg		fixed panels			2-axis tracking		
		RMSE (kWh/kWp/day)	MAE (kWh/kWp/day)	rMBE (%)	RMSE (kWh/kWp/day)	MAE (kWh/kWp/day)	rMBE (%)
All Days		0.24	0.18	2.1	0.99	0.81	15.2
Sunny (cloudless) Days		0.29	0.23	4.4	1.04	0.96	14.6
Sunny Days (average aerosol load)	aerosol-free	NaN	NaN	NaN	NaN	NaN	NaN
	aerosol-laden	NaN	NaN	NaN	NaN	NaN	NaN

73

74 **Table S10S8.** Evaluation metrics assessing the reliability of GSEE Climate Data Interface in
75 estimating total daily PV output power in Izana

STATION: Izana		fixed panels			2-axis tracking		
		RMSE (kWh/kWp/day)	MAE (kWh/kWp/day)	rMBE (%)	RMSE (kWh/kWp/day)	MAE (kWh/kWp/day)	rMBE (%)
All Days		0.28	0.23	3.4	1.12	0.94	11.2
Sunny (cloudless) Days		0.25	0.21	3.1	0.92	0.80	8.9
Sunny Days (average aerosol load)	aerosol-free	0.25	0.22	3.3	0.75	0.65	7.2
	aerosol-laden	0.24	0.19	2.3	1.38	1.31	15.3

76

77 ...

78

79

80 **Table S11S9.** Evaluations metrics accessing the reliability of using CAMS solar radiation time-
81 series for modelling PV output power in Carpentras

STATION: Carpentras		fixed panels			2-axis tracking		
		RMSE (Wh/kWp/hour)	MAE (Wh/kWp/hour)	rMBE (%)	RMSE (Wh/kWp/hour)	MAE (Wh/kWp/hour)	rMBE (%)
All-Sky scenes		49.7	36.6	3.9	60.7	43.0	3.8
All-Sky scenes (cloudiness)	cloud-free	35.9	28.4	3.2	41.7	32.5	2.7
	partly cloudy	74.1	56.7	5.7	94.2	70.3	7.1
	cloudy (overcast)	46.7	37.4	11.4	49.2	38.3	13.9
Cloudless- Sky scenes (aerosol load)	low	25.0	20.0	2.1	28.8	22.3	1.5
	moderate	32.5	25.9	3.4	36.7	29.1	2.9
	high	41.8	36.0	5.0	49.0	41.3	4.7
	very high	42.3	36.9	6.1	49.9	44.1	6.3

82

83 **Table S12S10.** Evaluations metrics accessing the reliability of using CAMS solar radiation time-
 84 series for modelling PV output power in Tamanrasset

STATION: Tamanrasset		fixed panels			2-axis tracking		
		RMSE (Wh/kWp/hour)	MAE (Wh/kWp/hour)	rMBE (%)	RMSE (Wh/kWp/hour)	MAE (Wh/kWp/hour)	rMBE (%)
All-Sky scenes		55.9	33.7	-1.0	75.2	46.1	-0.6
All-Sky scenes (cloudiness)	cloud-free	32.4	20.8	-0.7	45.2	29.8	-0.7
	partly cloudy	87.3	67.5	-4.4	111.8	86.9	-3.0
	cloudy (overcast)	124.9	89.2	23.3	210.7	151.6	48.1
Cloudless- Sky scenes (aerosol load)	low	16.6	11.9	0.3	20.8	15.3	-0.6
	moderate	19.7	14.9	-0.4	28.2	20.9	-1.2
	high	29.8	18.9	-0.9	34.9	23.2	-1.0
	very high	31.0	22.9	0.7	48.0	35.5	2.4

85

86 **Table S13S11.** Evaluations metrics accessing the reliability of using CAMS solar radiation time-
 87 series for modelling PV output power in Cener

STATION: Cener		fixed panels			2-axis tracking		
		RMSE (Wh/kWp/hour)	MAE (Wh/kWp/hour)	rMBE (%)	RMSE (Wh/kWp/hour)	MAE (Wh/kWp/hour)	rMBE (%)
All-Sky scenes		63.1	43.0	2.0	75.3	51.2	2.1
All-Sky scenes (cloudiness)	cloud-free	35.6	27.0	0.9	45.6	33.5	0.4
	partly cloudy	82.7	61.1	2.1	99.6	73.4	3.4
	cloudy (overcast)	77.3	50.8	20.7	83.5	53.4	24.8
Cloudless- Sky scenes (aerosol load)	clear sky / low	28.0	21.5	1.7	32.1	25.0	1.1
	moderate	38.5	30.4	2.8	48.3	38.8	2.3
	high	34.3	28.4	2.9	41.7	35.1	2.3
	very high	NaN	NaN	NaN	NaN	NaN	NaN

88

89

90 **Table S14S12.** Evaluations metrics accessing the reliability of using CAMS solar radiation time-
 91 series for modelling PV output power in Lindenberg

STATION: Lindenberg		fixed panels			2-axis tracking		
		RMSE (Wh/kWp/hour)	MAE (Wh/kWp/hour)	rMBE (%)	RMSE (Wh/kWp/hour)	MAE (Wh/kWp/hour)	rMBE (%)
All-Sky scenes		66.1	46.7	-1.2	76.2	53.8	-1.4
	cloud-free	37.9	24.9	-1.7	50.7	33.4	-2.5

All-Sky scenes (cloudiness)	partly cloudy	76.4	57.5	-2.6	88.9	67.0	-2.3
	cloudy (overcast)	60.9	42.3	8.0	63.9	43.2	9.5
Cloudless- Sky scenes (aerosol load)	clear sky / low	NaN	NaN	NaN	NaN	NaN	NaN
	moderate	42.3	28.7	-2.5	53.4	24.7	-3.0
	high	40.9	26.4	-2.4	52.6	32.0	-2.8
	very high	NaN	NaN	NaN	NaN	NaN	NaN